J. Condensed Matter Nucl. Sci. 27 (2018) 46–96

Research Article

Observation of Non-exponential Decay in X-ray and γ Emission Lines from Co-57

Florian Metzler, Peter Hagelstein*and Siyuan Lu

Massachusetts Institute of Technology, Cambridge, MA, USA

Abstract

On May 20, 2017, we started a series of experiments with the goal of observing vibrationally induced excitation transfer of the 14.4 keV nuclear state from excited Fe-57 to ground state Fe-57 nuclei. A steel plate with a Co-57 substrate on the front surface was vibrated by a piezoelectric transducer near 2.21 MHz; and emission in the X-ray region was recorded with an Amptek X-123 detector on the front side, a scintillator/photomultiplier detector on the back side, and a Geiger counter on the back side. The experiments provided a negative result for the originally sought ultrasonically induced excitation transfer effect, but instead showed non-exponential time histories for photon counts on all three detectors. Specifically, increased emission of the 14.4 keV gamma, Fe K_α and K_β X-rays was observed at early time. This enhancement was present at the start of the experiments at about 19% above expected levels for the 14.4 keV gamma, and about 17% for the Fe K-alpha, with the enhancement decaying away with a time constant of about 2.5 days. Emission on the Sn K_α was consistent with the expected exponential decay of Co-57 at the 1% level. Non-exponential decay with an enhancement at early time was also seen for the weak Fe K_α escape peak, and in the back-side Geiger counter data; and a reduction at early times was seen on the higher energy channels of the scintillator/photomultiplier detector counter both looking at the back side. The observed non-exponential decay is connected with the tightening of bolts on wooden clamps on the corners of the steel plate, which apply mechanical stress to the sample. Candidate interpretations are considered, in which the stress induced in the steel results in scattering and generation of THz phonons by dislocations, and in which phonon–nuclear coupling mediated by THz phonons leads to the transfer of nuclear excitation to other nuclei ("excitation transfer"), which can cause spatial delocalization of the source and angular anisotropy of the photon emission.
 ISSN 2227-3123

Keywords: Anomaly, Co-57, Excitation transfer, Non-exponential decay, Phonon–nuclear coupling

1. Introduction

The announcement of the excess heat effect in an electrochemical experiment with Pd in heavy water by Fleischmann and Pons in 1989 [1,2] was met with great skepticism, especially among physicists, in part because the effect was unexpected and seemingly impossible to reconcile with known nuclear physics and solid state physics. The many subsequent observations of the effect [3] support the contention that the excess heat effect is real, but more than 28

*Corresponding author. E-mail: plh@mit.edu.

 ISSN 2227-3123

years later, there is no accepted explanation as to why it might occur. Under normal conditions when a nuclear reaction produces energy, the resulting energy is carried off as energetic nuclear radiation. The absence of energetic nuclear radiation commensurate with the energy produced in the Fleischmann–Pons experiment provides reason for skepticism, and also provides a barrier to understanding the reaction mechanism [4]. For example, in an incoherent deuteron-deuteron fusion reaction it is possible to observe p+t and n+^{3}He to confirm the existence of the two dominant reaction pathways, and to measure the particle momenta and energies in order to shed light on the reaction kinematics. With no energetic reaction products associated with energy production in the Fleischmann–Pons experiment, a similar approach cannot be used to study the reaction mechanism. Because of this, it has been impossible to clarify unambiguously what nuclei are involved in Fleischmann–Pons experiments and derivative experiments, or how the reaction works (other than to say that it does not work like a conventional incoherent nuclear reaction).

Over the years there have been several hundred papers published describing a wide range of theoretical ideas as to how an excess heat effect might occur. Some of the proposals are in conflict with experiment as they predict energetic radiation. For those proposals which do not predict energetic radiation it is difficult to make an unambiguous connection with the Fleischmann–Pons experiment since they tend to involve mechanisms which have not been experimentally tested. Without independent experimental confirmation of at least some of the intermediate parts it is difficult to develop much confidence that any such model is correct. For example, we are currently interested in models based on a relativistic phonon–nuclear interaction [5], in which the absence of energetic nuclear radiation in Fleischmann–Pons type experiments is accounted for through the subdivision of 24 MeV quanta (the mass difference between D_2 and ^{4}He) to lower nuclear transitions, and eventually to down-conversion of the nuclear excitation into a commensurate number of phonons [6,7]. While the theoretical arguments seem strong, an unambiguous experimental confirmation of the underlying phonon–nuclear interaction and the resulting down-conversion effect is required.

Based on experience gained from the interaction of theory and experiment over the years since 1989, it seems clear that there will not be agreement on mechanism based on interpretations of results from Fleischmann–Pons type experiments alone. What is needed are different but related experiments, in which the same mechanisms are involved, but which permit an unambiguous interpretation [8]. We have previously advocated for up-conversion experiments, in which vibrations are up-converted to produce nuclear excitation, and we have interpreted collimated X-ray emission in the experiments of Karabut [9–17], and of Kornilova and coworkers [18–22], as due to the up-conversion of a commensurate number of vibrational quanta i.e. phonons.

Theory suggests that for phonon–nuclear coupling to be strong enough to show observable effects, the frequency of a vibrational mode ought to be as high as possible. However, suitable commercial sources for THz vibration excitation have not been available to us at the time of the reported experiments. Collimated X-ray emission in the Karabut experiment and in the Kornilova experiment suggest that observable effects may also occur at lower frequency vibrations. Cardone and coworkers have reported a variety of anomalies in experiments in which a steel bar is subject to vibrations at 20 kHz; including neutron emission [24–29] alpha emission [25,26,30–32], and elemental and isotopic anomalies [33–35] (see the reviews [36,37]). We interpret the observations of Cardone and coworkers as possibly resulting from up-conversion mechanisms at play. All of this suggested the possibility of observing effects from up-conversion in experiments with vibrations well below the THz regime.

Over recent years, we have been working toward experiments to experimentally investigate phonon–nuclear coupling and expected mechanisms and effects resulting from it. We tried earlier to make use of MHz vibrations to drive up-conversion in steel plates and excite ground state iron nuclei. In these up-conversion experiments, we sought – but did not find – collimated X-ray emission [38,39]. We have been able to drive metal plates up to 10 MHz. One set of up-conversion experiments involved high power piezoelectric transducers that have resonances near 2.2 MHz and could deliver over 100 W of vibrational energy to the plate [40]. We have also acquired and developed radiation detectors as diagnostics for changes in photon emission resulting from up-conversion and excitation transfer experiments. Moreover, in many of these experiments, compressional wooden clamps were applied to the edges of the sample plates,

so as to provide damping to the vibrations. This measure was motivated by the theoretical models suggesting that the presence of such damping could facilitate observable effects [61]. None of our conducted up-conversion experiments showed effects indicative of phonon–nuclear coupling at play. Consequently, we explored ways of increasing the chances of generating observable effects if they exist.

We have recently proposed an excitation transfer experiment, where phonon exchange with a highly excited vibrational mode transfers the excitation from excited nuclei to identical ground state nuclei located elsewhere [23]. Nuclear excited states in such an experiment originate from the decay of radioactive nuclei. Whereas an up-conversion experiment would require a high phonon–nuclear coupling strength to show observable effects, the newly proposed excitation transfer experiment would require a comparatively lower phonon–nuclear coupling strength and relatively minimal energy exchange with vibrations. Consequently, conditions for an excitation transfer experiment with observable effects are expected to be more easily and more likely created compared to conditions for an up-conversion experiment with observable effects.

In the Spring of 2017, we began the first set of excitation transfer experiments. In practice, these experiments differed from the earlier up-conversion experiments in that now the experimental setup included a constant source of short-lived iron nuclei in excited states. This was the case because of the presence, on the surface of the steel plate, of radioactive Co-57 which decays into excited Fe-57. The goal then was to look for effects resulting from the transfer of such given excitation to other nuclei (originally in ground state) during vibrational stimulation. The first series of experiments employed the above mentioned 2.2 MHz piezoelectric transducer for inducing vibrations. Each experiment lasted several hours. Compressional wooden clamps had been applied to the sample plate once at the beginning of the series of experiments and left in place. When considering the data of each of these experiments, the results appeared negative: We did not notice changes in photon emission correlated with vibrational stimulation.

However, when analyzing the entirety of acquired data across the full series of these early experiments, i.e. across several days, we did notice something unexpected: from the beginning of the series onward, the photon emission from the Fe-57 nuclear transition at 14.4 keV showed a non-exponential time history, as did the Fe K_α and K_β X-rays. We initially suspected a problem with the Amptek X-123 X-ray detector, but after further analysis we gained confidence that the X-123 detector functioned properly during the experiment (for example, the Sn K_α time history was consistent with normal exponential decay of the Co-57 at the percent level, and different detectors reported non-exponential time histories simultaneously).

After becoming aware of the unexpected observations across the series of shorter experiments from May 20-31, we began to consider the data across this period as representing a single exploratory experiment which we now refer to as the May 20 experiment. No physical change was made to the experimental setup of said May 20 experiment after applying the compressional clamps and placing the sample in front of detectors on May 20, 2017.

As a result of the unexpected observations, we were faced with an array of issues. Foremost among them: Is the effect real, or an artifact of the detectors or of the experiment? Also important is the interpretation of the observed effect: Why should there be a non-exponential time history, and what is the associated physical effect? Another question concerns the cause of the anomaly: The anomaly was present at the beginning of the experiment, which suggests that the cause was something that happened prior. This needed to be clarified, and many runs have since been carried out which help shed light on the experiment and effects observed. In such subsequent runs, the effect has been consistently observed (albeit comparatively weaker than in the first experiment) and these runs will be described in more detail in future reports.

In this initial paper, our focus will be primarily on the first observation of the anomaly, in part because it represents a critical milestone in this experimental campaign, and in part because much effort has gone into the analysis of the data. What follows is a detailed description of the experimental setup and resulting observations. At the end of this paper, we consider possible interpretations as well.

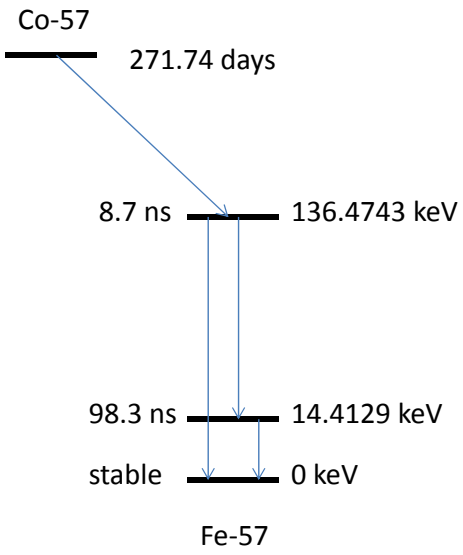

Figure 1. Simplified version of the nuclear decay scheme for Co-57; energy levels and half-life times are from the NUDAT2 online database of Brookhaven National Lab.

2. Beta Decay of Co-57, and Fe-57 Nuclear Levels

In the excitation transfer experiments introduced above, we use Co-57 to produce excited nuclear states of Fe-57. Excitation transfer effects are considered to affect the lowest two excited states of Fe-57 which are described in the following section. A brief review of some of the theoretical ideas associated with phonon–nuclear coupling, excitation transfer, and other mechanisms which motivate these experimental design choices is provided in Appendix A.

2.1. Co-57 beta decay scheme

A simplified version of the nuclear decay scheme of Co-57 [41–44] is illustrated in Fig. 1. Co-57 beta decays through electron capture, resulting 99.80% of the time [45] in the excited state of Fe-57 at 136.47 keV . A small fraction of the time, there is decay to higher energy Fe-57 states [46,47], which we will not concern ourselves with in what follows. The dominant gammas that result are the 14.4129 keV transition (which is widely used in Mössbauer studies), and two harder gamma transitions at 122.0614 keV and at 136.4743 keV.

2.2. Phonon exchange effects under consideration

We were most interested in the possibility of an excitation transfer effect involving the Fe-57 14.4 keV state, since the half-life is reasonably long (98.3 ns) and the transition energy reasonably low. An excitation transfer effect might manifest as delocalization through a decrease in the 14.4 keV gamma emission measured in the vicinity of the Co-57 source coinciding with an increase of such gamma emission elsewhere, or perhaps through collimation of the 14.4 keV gamma. Also possible might be an excitation transfer effect for the 136.5 keV state, but excitation transfer involving this state should be weaker compared to the lower state since the half-life is shorter (8.7 ns) and the transition energy is higher.

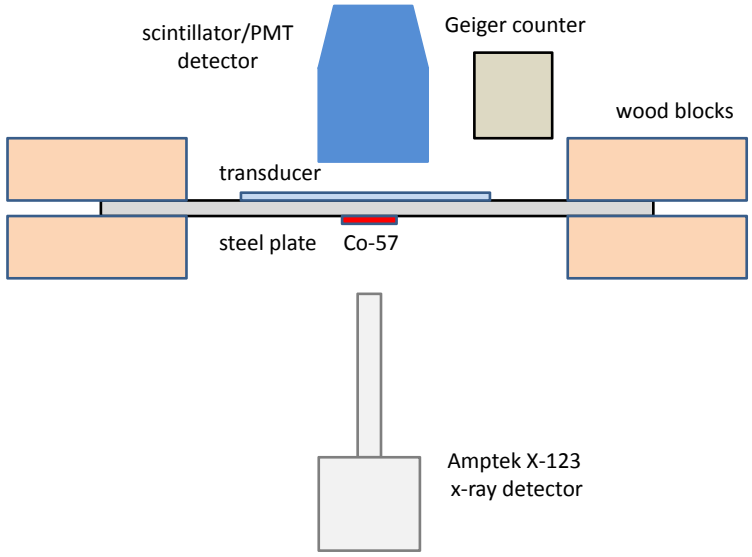

Figure 2. An idealized schematic of the experiment. The transducer is on top of the steel plate, with the Co-57 underneath. Wood blocks are clamped onto opposite corners (here idealized as sides) of the steel plate to add loss. The Amptek X-123 X-ray detector views the Co-57 from below; the scintillator/PMT detector views the sample from above, and the Geiger counter views the top side of the steel plate near a corner away from the Co-57.

3. Experimental Details, May 20 Experiment

As mentioned above, the initial goal of the experiment was to look for evidence of excitation transfer induced by vibrations near 2.21 MHz, generated with a piezoelectric transducer. The plan was to create a sample with excited state Fe-57 resulting from from the decay of Co-57, apply vibrations, and to look for a loss of the strength of the 14.4 keV nuclear transition at the site of the Co-57 when vibrations are present.

3.1. Experimental setup

A simplified schematic of the experiment is shown in Fig. 2, indicating the primary elements of the experimental configuration (details concerning individual elements follow below). Four pieces of plywood were bolted down on opposite corners of the steel plate to provide loss [40]. Three holes were drilled in each piece of plywood for bolts, and nuts were screwed on with a torque wrench, resulting in compressional stress on the plate of approximately 2000 lbsf. As described below, Co-57 was placed on the front side of the steel plate through evaporation of an acid solution, with the front side facing down in the figure, above a coarse aluminum protective mesh (not shown in the schematic), with the Amptek X-123 X-ray detector below. The scintillator/PMT detector looks down on the back side, off to the side of the transducer. The Geiger counter also views the back side of the steel from above, oriented over a free corner away from the Co-57. A side-view photograph of the steel plate, wood clamps, and detectors is shown in Fig. 3.

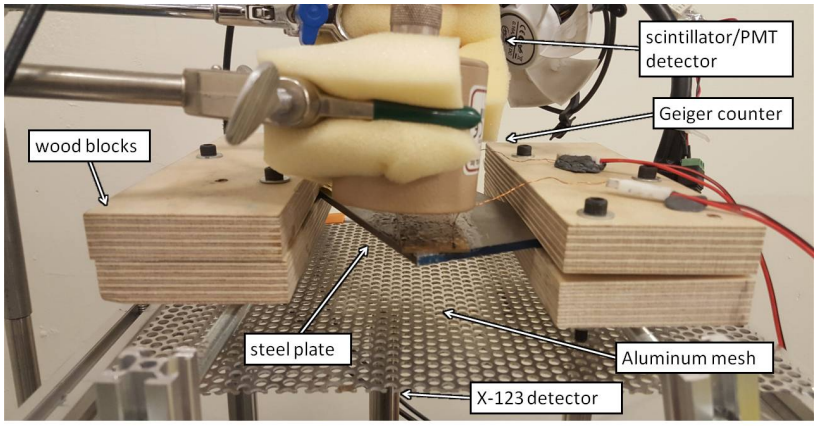

Figure 3. Experimental setup. Four plywood clamps are tightly bolted onto the steel plate, which rests on a rigid rack for support. Below is a protective coarse aluminum mesh which rests on an aluminum frame. Below the aluminum mesh is the Amptek X-123 X-ray detector, which rests on foam (not shown) to minimize vibrational coupling. Above the steel plate on top of the corner of the steel plate is the Geiger counter in a holder with foam. Behind the Geiger counter is a scintillator/PMT X-ray detector.

3.2. Steel plate

We used a 3"×6"×5/32" steel plate made of low-carbon steel (McMaster-Carr part number 1388K546) shown in Fig. 4. The uppermost peak of the $n = 3$ fundamental resonance for this (loaded) plate is observed around 2.22 MHz (Fig. 5), slightly below the transducer resonance (the resonance of this transducer is a bit higher than for the one discussed in Ref. [40]). The corresponding longitudinal sound speed of steel estimated from this frequency is 5.870×10^5 cm/s with an uncertainly on the order of 1% due to variations present in the thickness of the plate.

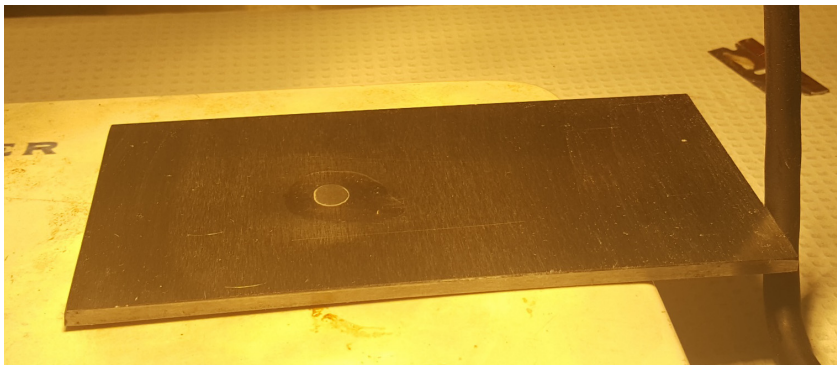

Figure 4. Steel plate sample with 200 μCi of evaporated Co-57.

3.3. Co-57

We obtained 1000 μCi of $^{57}CoCl_2$ from Eckert & Ziegler, in 0.1 M HCl, which came as 0.15 ml of solution in a 0.3 ml vial in November 2016. Roughly 1/3 was evaporated onto the steel (which involved using a micropipette to move some of the solution from the vial to the steel plate, and then waiting on the order of an hour for evaporation in air). The half-life of Co-57 is 271.74 days, so by the time of the May 20 experiment there was roughly 200 μCi remaining on the plate. The evaporated solution was covered by epoxy (J-B Weld 50112 Clear 25 ml ClearWeld Quick-Setting Epoxy Syringe) in order to prevent flaking off or physical loss of Co-57 activity. A ring-shaped residue is present at the end of the evaporation. The size of the evaporated region can be seen in Fig. 4 as the small whitish region approximately 1 cm in diameter, and the epoxy covering can be seen as the clear layer approximately 3 cm in diameter over and surrounding the evaporated region.

3.4. Transducer and gel

Ultrasonic vibrations were driven by a high-power 1"×6.5" piezoelectric transducer rated for 1.95–2.07 MHz from PCT Systems Inc. For unloaded low power operation at room temperature on Styrofoam, and for operation on steel, the transducer's resonance was found to be slightly higher than rated (approximately 2.26 MHz). For mechanical coupling of the transducer to the steel we used VersaSonic multipurpose high temperature ultrasonic couplant from ECHO Ultrasonics. The piezo crystal was driven by an E&I A150 Broadband Power Amplifier through an Amplifier Research DC2600A dual directional coupler. When the transducer was driven we made use of a 20% duty cycle to avoid high temperature in the piezo crystal. The electrical power reported in Fig. 5, and later on in the paper, refers to the peak (and not average) power.

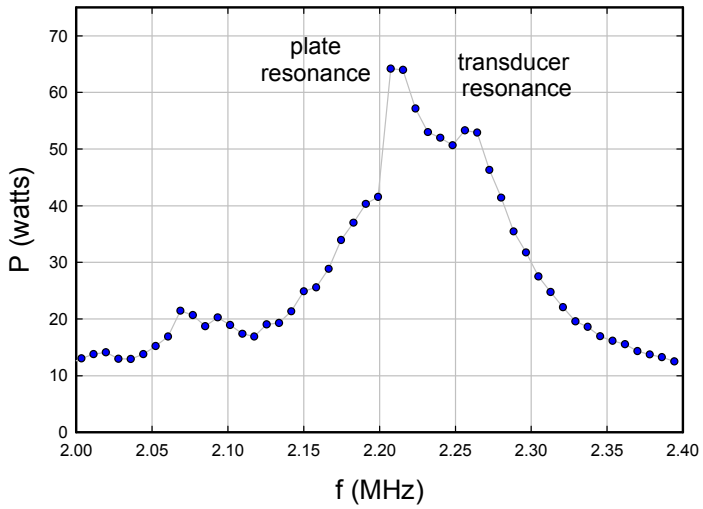

Figure 5. Electrical power to the transducer as a function of frequency for one of the transducer drive periods for the May 20 experiment.

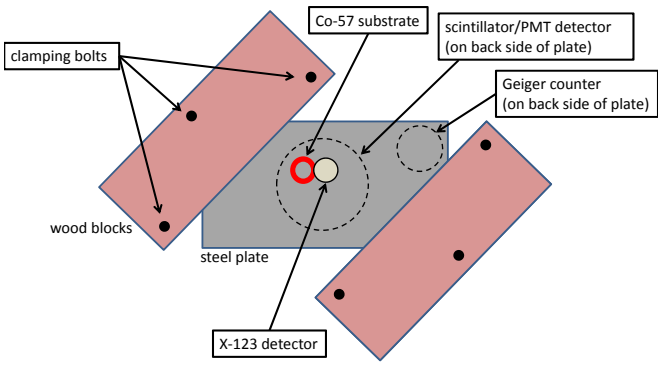

Figure 6. Steel plate (*light gray*); plywood clamps (*brown*); locations of bolts (*black*); there was one location for the evaporated Co-57, with four positions possible indicated by the red circles.

3.5. Clamps on steel plate

An effort was made after the May 20 experiment to determine the arrangement of the plywood clamps on the steel plate. From this reconstruction a layout was drawn to provide an approximate indication (see Fig. 6). The position of the plywood clamps on the steel could be determined from the residual indentations in the wood, and the locations of the bolt holes are available from photographs; these are indicated in the figure. The Co-57 evaporation is off-center, and the closest distance between the Co-57 and the nearest clamp edge is 1.22 in.

3.6. Aluminum mesh

There was a coarse aluminum mesh between the steel plate and the Amptek X-123 detector which we installed in order to provide protection for the thin Be window of the detector. This mesh is sold by McMaster-Carr (part number 9232T191) as Aluminum Perforated Sheet, 0.063" thick with 0.1875" diameter holes and 51% open area. It is made out of 3003 aluminum.

3.7. X-123 X-ray detector

For X-ray and gamma detection on the front side of the plate (facing the radioactive source) we used a 500 μm Amptek X-123 Si-PIN detector with a 0.5 mil Be window and 6 mm^2 area. For the data discussed in this paper we used spectra recorded every minute and logged with a time stamp. We used 2048 bins up to a maximum energy near 28 keV.

For data analysis, the energy band time history data presented later in the paper consists of summed up counts over 40 bins (525 eV) for the Fe K_α and Fe K_β lines, and 60 bins (788 eV) for the Fe-57 14.4 keV line. For the Sn K_α line 69 bins (906 eV) were used, and for the Sb K_α line 43 bins (564 eV) were used.

3.8. Scintillator/PMT X-ray detector

On the back side of the plate (not facing the radioactive source) we used a scintillator/photomultiplier detector for X-ray and gamma detection. This detector uses a 250 μm ZnS scintillator (normally used for alpha detection) and a Hamamatsu 3" photomultiplier tube (PMT), model R6233, with a thin radfilm cover to block visible light. This

detector was built by iRad Inc in Florida. The PMT was operated with a GS-2000-PRO driver from Bee Research. The analog output went into a Focusrite 192 kHz low-noise USB audio interface and was analyzed with open source Theremino MCA software. The 2048 channel spectrum was recorded once every minute with a time and date stamp.

3.9. Geiger counter

We made use of a Ludlum Geiger counter with a Model 44-88 Alpha Beta Gamma detector probe, and with a Ludlum 2350-1 Data Logger, to detect radiation on the back side. The Ludlum system develops an estimate for the count rate per minute roughly each half second, and the rate was logged roughly once each second with a time and date stamp.

3.10. Neutron detector

A Wendi-2 neutron detector from Thermo Fisher was placed next to the experimental assembly to monitor for possible neutron emission during the experiment.

4. Experimental results: shorter runs with MHz Vibrations

As mentioned in the introduction, the goal of the experiment was to test whether vibrations induced by the piezoelectric transducer could cause excitation transfer of the Fe-57 14.4 keV excited state population. We began with runs driving the transducer at high power (approximately 150 Watt); however, we were concerned that the detectors might be seeing noise due to the high current level used to power the transducer, so in later runs we reduced the transducer power and

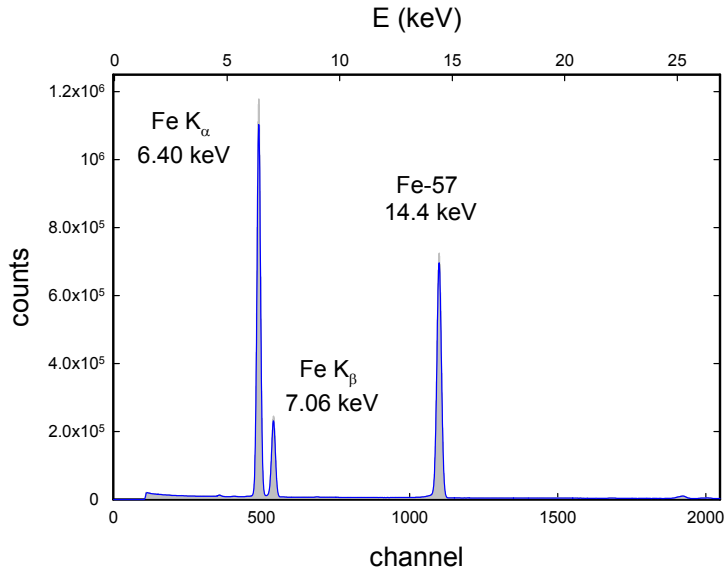

Figure 7. Time-integrated spectrum for first part of the experiment (20–23 May); raw counts per channel (*grey histogram*); averaged spectrum (*blue line*).

increased the duty cycle at which the transducer was driven (to 25% and 30%). Results from the low power run are considered in this section. Results for the entire period covering all runs, i.e. what we now refer to collectively as the May 20 experiment, are discussed from Section 5 onward.

4.1. Time-integrated X-ray spectrum

The primary diagnostic in this experiment is the Amptek X-123 detector, so we begin by considering the X-ray and gamma lines from this detector. The X-123 spectrum integrated over the first few days (5/20/17 14:48 to 5/23/17 06:50) of the experiment is shown in Fig. 7. A discussion of the calibration of the X-123 spectrum is given in Appendix B, along with line identifications in the spectra.

The 14.4 keV gamma line shows up clearly in the middle of the spectrum; and at lower energy, the lines resulting from the Fe K_α and Fe K_β transitions are very strong. There is the possibility of Fe K_α or Fe K_β radiative decay following the initial electron capture by Co-57; subsequently, there is a substantial probability of Fe K_α or Fe K_β radiative decay following the nonradiative decay of the 14.4 keV state by internal conversion [48–50].

4.2. Excitation transfer test with moderate transducer power

The test for excitation transfer – as initially envisioned – involved the prediction of a prompt reduction in the 14.4 keV gamma line while ultrasonic vibrations were generated via the piezoelectric transducer. In Fig. 8 we show the time history of counts per hour for the 14.4 keV line along with the peak transducer power. To construct this plot we summed the counts taken and logged each minute to develop one hour totals, which are plotted at the time of the last minute of the accumulation, relative to the start of the first day of the May 20 experiment. In this plot, as well as in other plots in this paper, no background subtraction is applied.

The figure suggests that there is no significant dip in the emission when the transducer is driven, as had been considered. If there is a more general response of the emission strength to the vibrations, it is not particularly obvious from this data set; however, we will revisit this question in connection with higher power operation later on in Section 7.

5. Experimental results: entire May 20 experiment, Amptek X-123 data

When considering the entirety of the May 20-31 period – as opposed to the shorter runs considered in the previous section – we observed non-exponential decay for the principal emission lines most clearly in the Amptek data. Before we examine time histories for lines with non-exponential time dependence below, we first consider observations of some weaker high energy lines that are consistent with exponential decay.

5.1. Weaker lines in the spectrum

In Fig. 7 we focused on the strong lines normally seen from the beta decay of Co-57, and now we are interested in the weaker lines in the spectrum. A logarithmic version of the time-integrated spectrum is shown in Fig. 9 in which we can see several weaker lines. We have marked the Fe K_α escape peak at 4.51 keV, as well as the Sn K_α at 25.2 keV. Above the Sn K_α there is a line (unmarked) at 26.3 keV which is the Sb K_α. Just below the 14.4 keV gamma is an escape peak for the 14.4 keV gamma.

5.2. Decay of the Sn K_α X-ray line

The steel plate contains a small amount of Sn, as we verified by X-ray fluorescence (XRF) measurements of an equivalent steel plate ordered from the same supplier. This line is relevant since it is present as a result of ionization

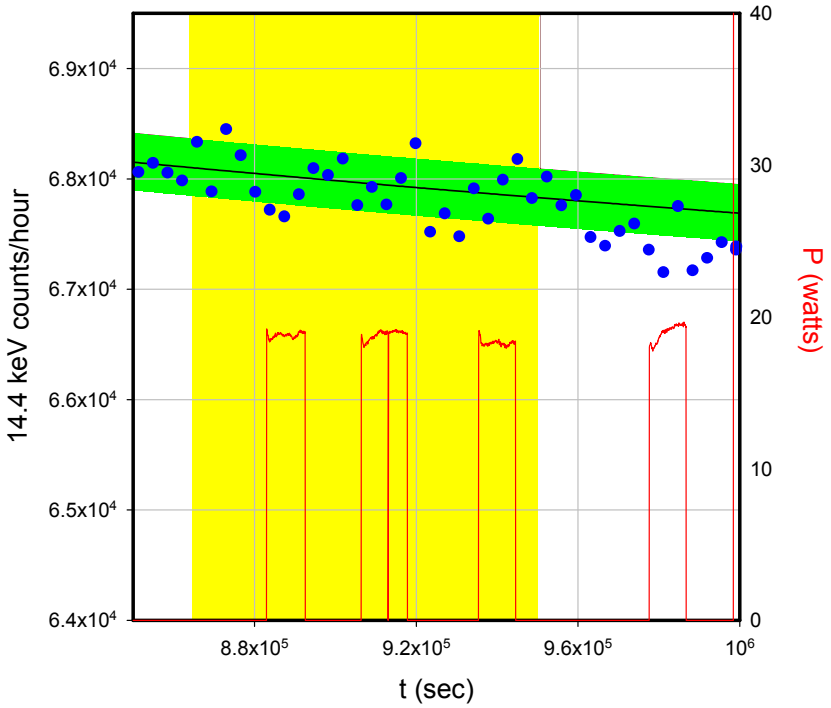

Figure 8. Counts on the Fe-57 nuclear transition at 14.4 keV as a function of time (*blue*); global empirical model (described in the following section) fit to the data (*black*); $\pm 1\sigma$ region determined by the square root of counts based on empirical model (*green area*); transducer power (*red*). Time in seconds indicated at the bottom; days between 5/29 and 5/31 indicated by the yellow and white background (each color band marks one day).

due to the harder 122.1 and 136.5 keV gammas of the 136.5 keV state initially populated by the decay of Co-57. Because of this, we can learn something frm the Sn K_α line about the dynamics of the 136.5 keV state indirectly, since in this experiment we do not have direct measurements of the harder gammas. The results are shown in Fig. 10. We see that the time history is consistent with the 271.74 day half-life exponential decay at the level of about 1%.

The arrival of counts during an accumulation time is governed by Poisson statistics, so that the standard deviation is the square root of the number of counts. While we have available spectra taken once per minute, the scatter of the resulting time history is sufficiently large as to be uninteresting. We have summed over 6 h of these one minute spectra (with the total plotted at the end of the 6-hour period in each case) in order to reduce the scatter.

5.3. Decay of the Sb K_α X-ray line

As mentioned above, there is a weak X-ray line above the Sn K_α that we identify as the Sb K_α (see Appendix B). From the same steel XRF measurements mentioned in Section 5.2 for Sn, we found also that Sb is present. We would expect to see a similar decay on this line as for the Sn K_α, since both the Sn and Sb K_α lines result from photoionization due

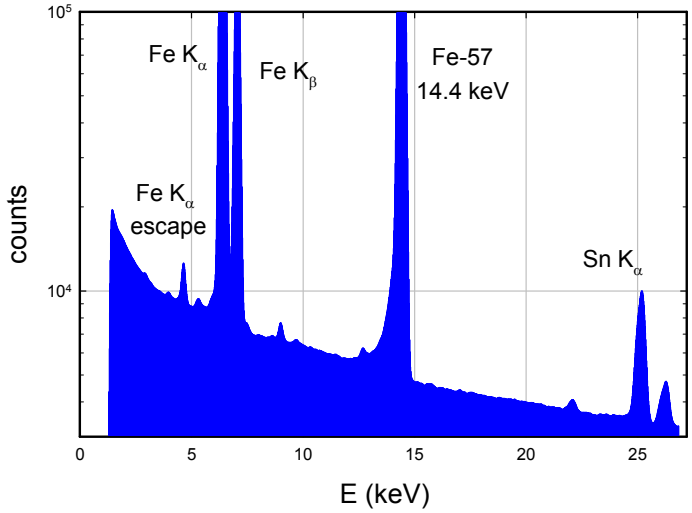

Figure 9. Time-integrated spectrum for first part (20–23 May) part of the run; raw counts (*blue histogram*).

to the harder gammas. In Fig. 11 is shown the time history, and we see that the decay on this line is consistent with 271.74 day half-life exponential decay at the level of about 1.5%. Note that in this case, there are more counts due to the "background" than due to Sb K_α X-rays (see Fig. 9); however, since the "background" in this case is due to the detector response to the harder gammas, we would expect a similar time history for both contributions. The spread is a bit larger compared to the Sn K_α since the signal is weaker.

5.4. Non-exponential decay of the 14.4 keV gamma line

The 14.4 keV gamma line in this experiment shows a non-exponential decay (see Fig. 12). This result was not expected, and has been the source of astonishment and much discussion. We interpret the faster-than-exponential decay observation to be due to an enhancement of the signal at early time, instead of due to accelerated decay of Co-57 (which would be inconsistent with the Sn K_α and Sb K_α time histories present in the sections above).

For this plot, and for those that follow, we made use of an empirical model given by

$$\ln I(t) \;=\; -\frac{t}{\tau} + a + b\,\mathrm{e}^{-t/\tau_0} \tag{1}$$

with $\tau = 271.74/\ln 2$ days from the NUDAT2 database. From this model we can estimate the intensity expected if no anomaly were present from

$$\ln I_0(t) \;=\; -\frac{t}{\tau} + a. \tag{2}$$

From a least squares fitting of the model parameters to the data we find

$$\tau_0 \;=\; 2.18 \times 10^5\ \mathrm{s}, \tag{3}$$

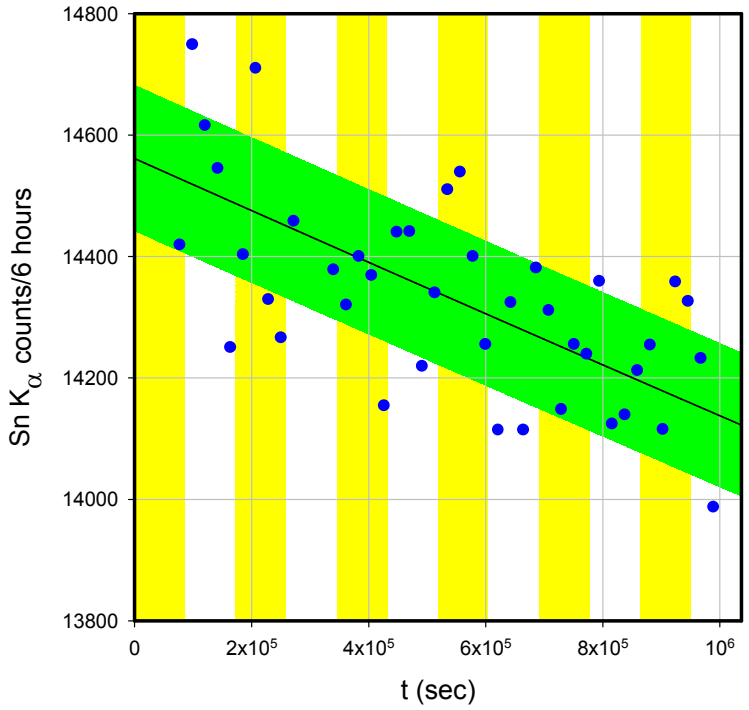

Figure 10. Time history of the of the Sn K_α transition (*blue circles*); exponential decay with 271.74 days half-life (*black*); $\pm 1\sigma$ error bars determined by the square root of the average number of counts (*light green solid region*). The bottom time axis is in seconds; the alternating yellow and white background show the duration of each day between 5/20 and 5/31.

which is a time constant associated with the physical configuration of the experiment, and not with any fundamental nuclear process. We see in Fig. 12 that this empirical model provides a good fit to the data.

5.5. Spectrum near the 14.4 keV gamma line as a function of time

If the enhancement of 14.4 keV excited states of Fe-57 were created through some new process, there might be the possibility of a modification in the line shape. Note that since the line is instrument broadened (FWHM of 220 eV for this line with the Amptek X-123 detector), such an effect would need to be very large in order to be seen with this kind of measurement. This provides us with the motivation to examine the spectrum in the vicinity of the 14.4 keV line up close. The spectrum as a function of time is shown in Fig. 13. We summed 30 min of data for each data point used in this plot. We see some data loss near 300 000 s, and we can see clearly that the line is brighter at early times in the experiment. There seems to be a minor drift in the relative channel average (on the order of a few tenths of a channel, or 2–3 eV at 14.4 keV), which may be due in part to a small drift in the detector gain (since the dynamics of the average relative channel is similar for the 14.4 keV X-ray and Fe K_α gamma). There does not appear to be a significant change in the line shape observed with the X-123 at early time in this data.

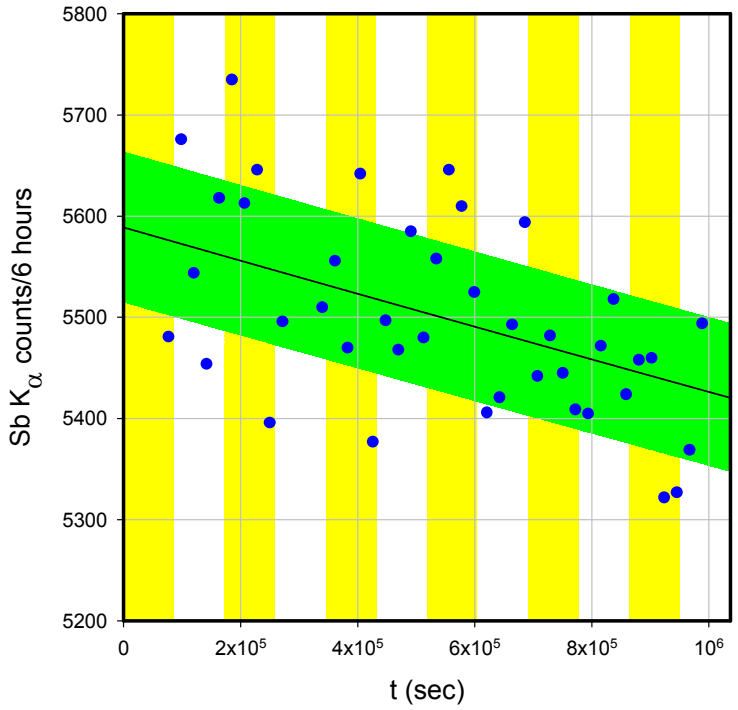

Figure 11. Time history of the of the Sb K_α transition (*blue circles*); exponential decay with 271.74 days half-life (black); $\pm 1\sigma$ error bars determined by the square root of the average number of counts (*light green solid region*). The bottom time axis is in seconds; the alternating yellow and white background show the duration of each day between 5/20 and 5/31.

5.6. Non-exponential decay of the Fe K_α X-ray line

A similar non-exponential decay history is observed also for the Fe K_α X-ray, as shown in Fig. 14. We would expect internal conversion of the 14.4 keV nuclear state to lead to Fe K_α emission, so it does not come as a surprise that we should see a qualitatively similar anomaly in the Fe K_α emission (note that there is also a contribution to the Fe K_α emission following the initial Co-57 capture). We again fit to the empirical model above, with a time constant parameter of

$$\tau_0 \;=\; 2.16 \times 10^5 \text{ s}, \tag{4}$$

which is within about 1% of what was found for the 14.4 keV gamma transition above.

5.7. Non-exponential decay of the Fe K_β X-ray

We observe similar dynamics on the Fe K_β transition as shown in Fig. 15 (as expected since the mechanism of Fe K_β emission is very similar to that for Fe K_α). The time constant parameter in this case is similar to the previous cases

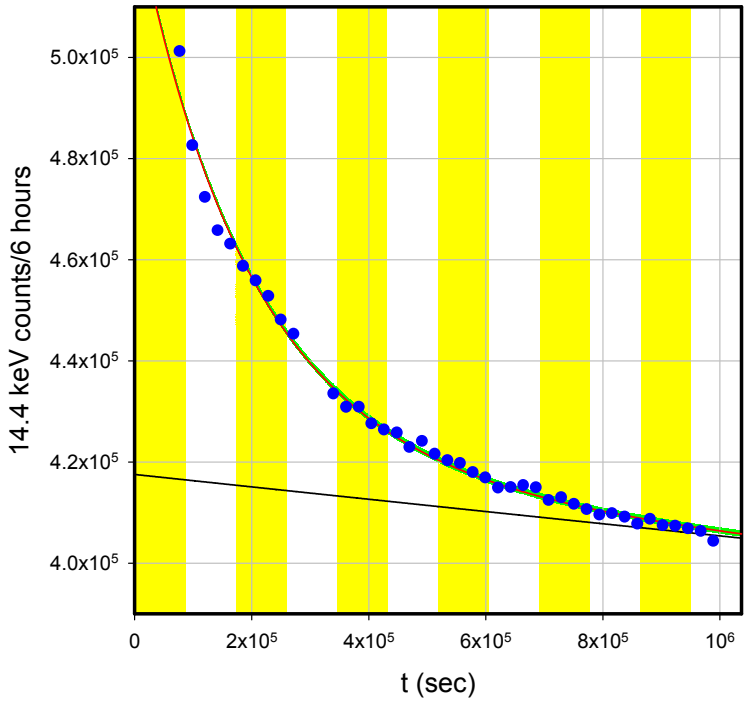

Figure 12. Time history of the of the Fe-57 nuclear transition at 14.4129 keV (*blue circles*); empirical model (*red*); exponential decay with 271.74 day half life consistent with empirical model (*black*); the $\pm 1\sigma$ error bars determined by the square root of the average number of counts (*light green solid region*) is sufficiently narrow to be obscured by the red line of the empirical model. The bottom time axis is in seconds; the alternating yellow and white background show the duration of each day between 5/20 and 5/31.

$$\tau_0 \;=\; 2.23 \times 10^5 \text{ s}. \tag{5}$$

5.8. Non-exponential decay for the Fe K_α escape peak

We would expect to see the same non-exponential decay time history in the Fe K_α escape peak as in the Fe K_α X-ray; however, since the escape peak is much weaker, the competing contribution from the "background" due to the harder gammas (which decay exponentially) leads to a dilution of the effect. We analyzed the dynamics of the emission from this line (see Fig. 16) with the result that there is a non-exponential component that is less pronounced than for Fe K_α. For the model used in Fig. 16 we used $\tau_0 = 2.16 \times 10^5$ s value from the Fe K_α fit. As mentioned above, no background subtraction was done for this line. There again is more relative spread in the data since the count rate is much lower.

The decay of the signal is compatible with the time constant τ_0 of the Fe-57 14.4 keV gamma and Fe K_α and K_β X-ray lines. Due to the weakness of the line, the spread is large, so that the Fe K_α escape data does not provide a strong constraint on τ_0.

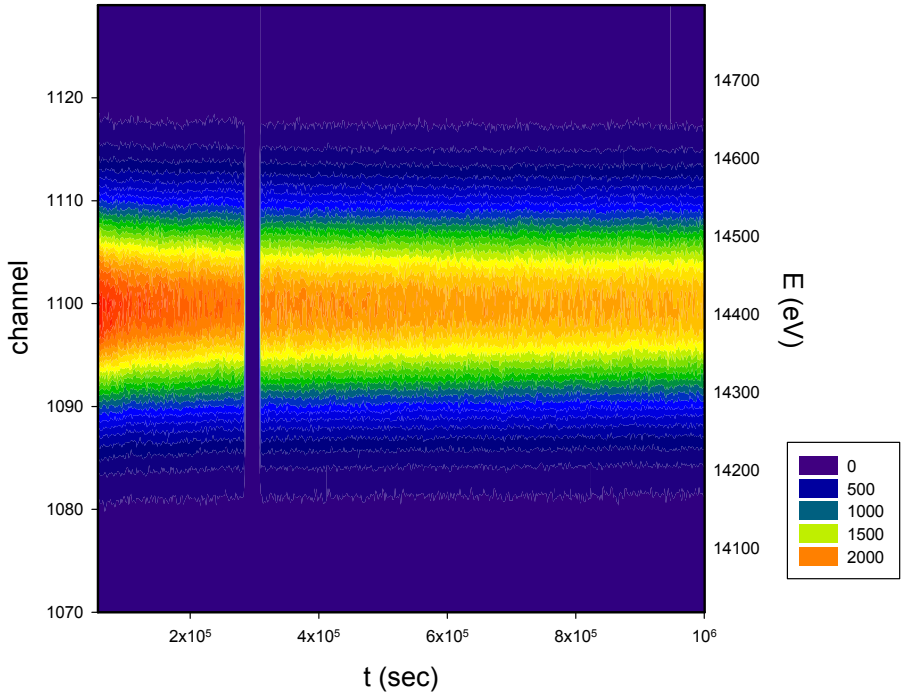

Figure 13. Time history (counts per 30 min) of the spectrum of the Fe-57 nuclear transition at 14.4129 keV; the time axis (*bottom*) is in seconds; the channel number is on the left and the energy is on the right.

6. Experimental results: entire May 20 experiment, data from other detectors

In this section, we are interested in results from the Geiger counter, from the scintillator/PMT detector, and also from the neutron detector. The neutron detector did not exhibit an unexpected dynamical time history, but unexpected non-exponential decays were recorded on the other detectors.

6.1. Non-exponential decay of the Geiger counter signal

The Geiger counter was pointed at the back side of the steel plate, and the plate is sufficiently thick that there is no possibility of the 14.4 keV gamma or the Fe K_α, K_β X-rays from the Co-57 making it through the plate without being absorbed. Consequently, only the harder 122.1 and 136.5 keV gammas (and the much weaker gammas at even higher energy) from the Co-57 make it to the back side. In this experiment the Geiger counter is relatively distant from the Co-57 source, so that the signal strength due to the Co-57 is reduced by a factor of about 50 from what is measured in close proximity. Now, we know from the Sn K_α signal that the time history of the 122.1 and 136.5 keV gammas as determined by the Sn K_α proxy does not show a strong early time enhancement. Consequently, the non-exponential decay of the Geiger counter signal shown in Fig. 17 is providing new information not available from the front side X-123 data.

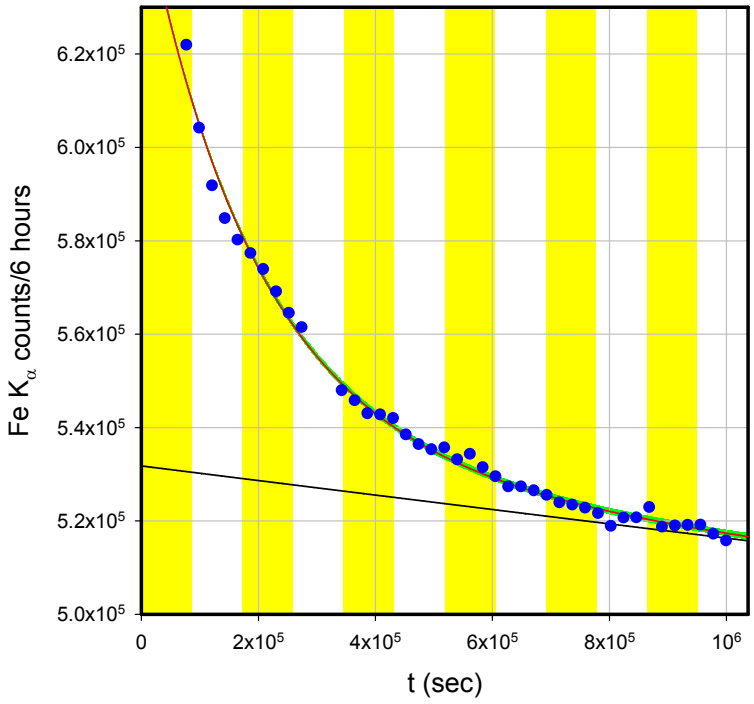

Figure 14. Time history of the of the Fe K_α X-ray (*blue circles*); empirical model (*red*); exponential decay with 271.74 days half-life consistent with empirical model (*black*); the $\pm 1\sigma$ error bars determined by the square root of the average number of counts (*light green solid region*) is sufficiently narrow to be obscured by the black line of the empirical model. The bottom time axis is in seconds; the alternating yellow and white background show the duration of each day between 5/20 and 5/31.

Because the May 20 experiment was not originally conceived as a single experiment but rather as a series of shorter runs, Geiger counter data was not taken throughout the entire May 20-31 period, resulting in a significant gap and fewer data points to work with. Nevertheless, it is clear that the decay in this case is very much non-exponential. We have fit the available data points, accumulated as above, to the empirical model once again. The optimization of the model leads to a value for τ_0 of

$$\tau_0 \;=\; 2.930 \times 10^5 \text{ s}, \tag{6}$$

We note that the fluctuations in this case are larger than what would be expected from the total counts per 30 min. One contributing reason for this is that an estimate for the counts per second determined by the Geiger counter system was stored only approximately once per second, instead of twice per second as the system records internally.

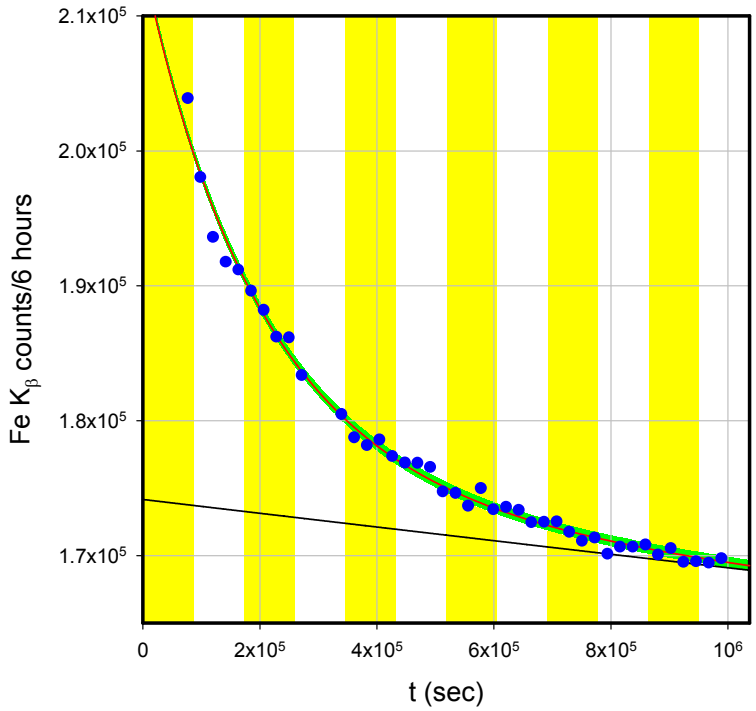

Figure 15. Time history of the of the Fe K_β X-ray (*blue circles*); empirical model (*red*); exponential decay with 271.74 days half-life consistent with empirical model (*black*); the $\pm 1\sigma$ error bars determined by the square root of the average number of counts (*light green solid region*). The bottom time axis is in seconds; the alternating yellow and white background show the duration of each day between 5/20 and 5/31.

6.2. Results for the scintillator/PMT detector

We recall that the scintillator/PMT detector is also located on the back side (not facing the Co-57 substrate). At the time of the May 20 experiment, the driver of the scintillator/PMT detector was still occasionally plagued by interruptions (with a sudden on and later sudden off time characteristic) during which noise in the form of pulses with a very long decay time was added to the signal. Nevertheless, much of the data from this detector is intact, and in some of the channels there appears to be a distinct non-exponential signal. Here we have chosen to display the data sets (analyzed using accumulation based on the same approach as for the other data) including periods containing obvious interruptions since a unique systematic retrospective separation of the data and interruption noise is not possible.

The most straightforward data set is the summed channels corresponding roughly to the 1–2 keV range. The time history is seen to be consistent with exponential (aside from interruptions) for the 271.74 day beta decay half-life of Co-57, as shown in Fig. 18. The sharp excursions up to the vicinity of 5000 counts per 30 min are interruption noise, as are the excursions down below 4000 counts/30 min. For these channels the aluminum in the radfilm covering the scintillator in strongly absorptive, so that few soft X-rays get through and register. In the presence of lower energy sources this detector gives a spectrum with a shape consistent with Al X-ray fluorescence, where the aluminum in the radfilm may be radiating inefficiently. There may be contributions to the signal also from the harder gammas incident

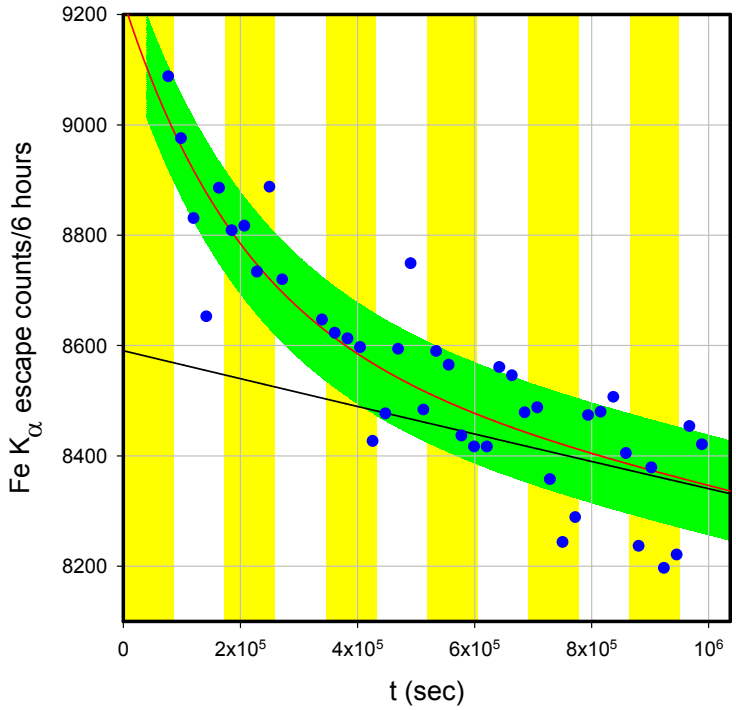

Figure 16. Time history of the of the Fe K_α escape peak (*blue circles*); empirical model (*red*); exponential decay with 271.74 days half-life consistent with empirical model (*black*); the $\pm 1\sigma$ error bars determined by the square root of the average number of counts (*light green solid region*). The bottom time axis is in seconds; the alternating yellow and white background show the duration of each day between 5/20 and 5/31.

in other parts of the detector.

In Fig. 19 we show the time history of the summed channels between 2 and 4 keV, along with a parabolic model curve to guide the eye. Due to the poor energy resolution of the scintillator/PMT detector, we would expect minor contributions from the Fe K_α to appear in these channels. Once again the fast excursions above 140 000 counts/30 min are interruption noise, as are the excursions below 130 000 counts/30 min. We see a non-exponential decay with a qualitatively different dynamics than what was seen on the front side by the Amptek X-123 and on the edge of the back plate by the Geiger counter.

The time history for the summed scintillator/PMT channels between 4 and 10 keV are shown in Fig. 20. These channels were selected to capture the bulk of the Fe K_α and K_β lines, should such emission occur keeping in mind that all Fe K_α and K_β emission originating from the front side is absorbed by the plate, but there is some XRF due to the harder gammas. We see again a roughly parabolic signal with interruption noise present. The early fast excursions up to 1.1×10^6 counts/30 min and the later excursions down below 9.8×10^5 counts/30 min are due to the interruption noise.

The time history for the summed channels between 10 and 20 keV is shown in Fig. 21, also with a parabolic curve that approximates the signal in the absence of the interruptions. The intent of this set of channels was to capture what

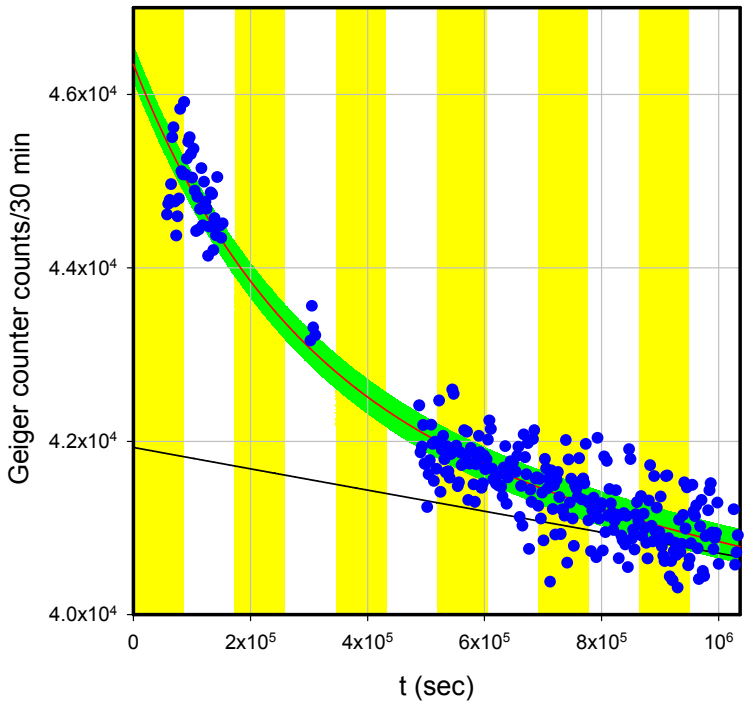

Figure 17. Time history of the of the Geiger counter signal (*blue circles*); empirical model (*red*); exponential decay with 271.74 days half-life consistent with empirical model (*black*); the $\pm 1\sigma$ error bars determined by the square root of the average number of counts (*light green solid region*). The bottom time axis is in seconds; the alternating yellow and white background show the duration of each day between 5/20 and 5/31.

was going on in the general vicinity of the 14.4 keV gamma ray (as yet we have not seen 14.4 keV emission on the back side in other experiments with good spectral resolution). A roughly parabolic response is evident, and the occasional large downward excursions are due to the interruption noise. We note that there are fluctuations present in the data well beyond what would be expected from Poisson statistics.

Finally, the time history for the uppermost channels above 20 keV is shown in Fig. 22, which shows a similar trend to the other channels. We see a parabolic signal with a few sharp downward excursions due to interruption noise.

At the time of writing this text, the occasional interruptions and resulting noise exhibited by this detector have been addressed. Despite the less than ideal condition of the data taken with this detector during the May 20 experiment, we chose to report the data here with the caveats mentioned above.

6.3. Neutron counts

Data from the neutron detector is shown in Fig. 23. We see that the total number of counts per six hours is low, so that the statistical fluctuations are relatively large compared to the average count rate. The average count rate is 64.9 counts per 6 hours which is equivalent to 3.00×10^{-3} counts/s. Given the listed efficiency of the detector which is 0.84 cps/μSv/h, the average background count rate is then 3.6 nSv/h. This data set is consistent with no incremental

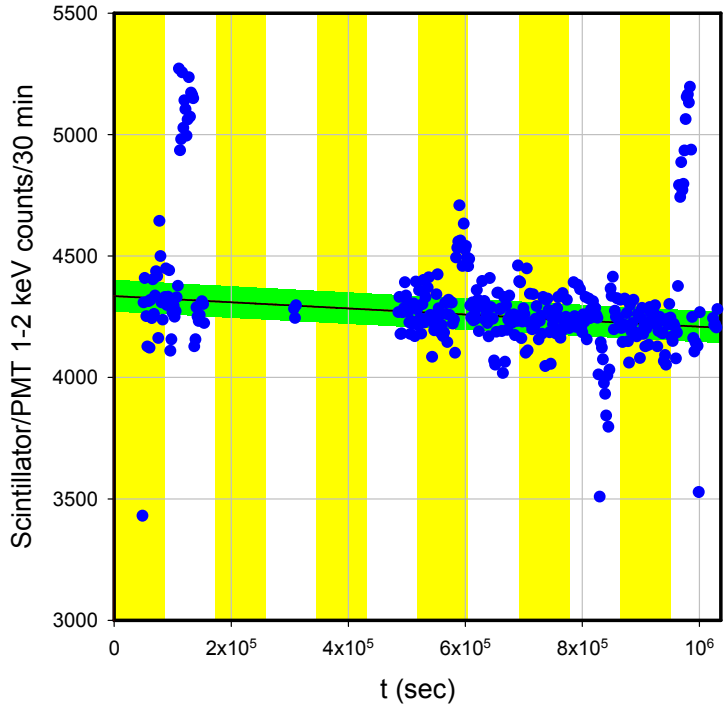

Figure 18. Time history of the of the 1–2 keV channel of the scintillator/PMT detector (*blue circles*); empirical model (*red*); exponential decay with 271.74 days half-life consistent with empirical model (*black*); the $\pm 1\sigma$ error bars determined by the square root of the average number of counts (*light green solid region*). The bottom time axis is in seconds; the alternating yellow and white background show the duration of each day between 5/20 and 5/31.

neutron emission during the experiment with a 1 σ upper limit of 0.44 nSv/h.

7. Basic Considerations

Non-exponential decay observed for the 14.4 keV gamma line, and for the Fe K_α and K_β X-ray lines, by the front-side Amptek X-123 detector, appears to us to be anomalous. Some support for such an assertion is provided by a similar time history for the back-side Geiger counter away from the Co-57, even though the origin of the back side Geiger counter signal must be different. The scintillator/PMT detector on the back side near the Co-57 reports a different (early reduction instead of enhancement) and slower non-exponential decay.

It could be argued that any interpretation is premature: since the May 20 experiment was the first of its kind; since the effects seen in subsequent experiments were weaker; and since some colleagues may view the results presented in this paper as artifacts. The thought here is that it is appropriate to discuss both possible sources of problems (which should be addressed in subsequent experiments), and also to discuss possible interpretations (which might point to future experiments that might provide clarification and confirmation). In this section we focus on some basic issues. With respect to interpretation, one hypothesis based on delocalization of the nuclear excitation as a result of excitation

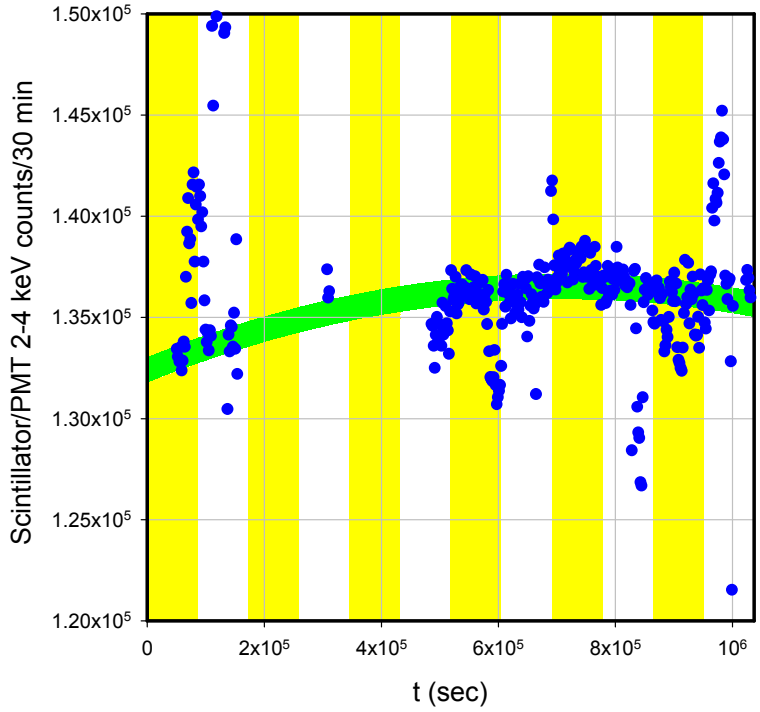

Figure 19. Time history of the of the 2–4 keV channel of the scintillator/PMT detector (*blue circles*); simple parabolic model (*red*); the $\pm 1\sigma$ error bars determined by the square root of the average number of counts (*light green solid region*). The bottom time axis is in seconds; the alternating yellow and white background show the duration of each day between 5/20 and 5/31.

transfer is discussed in Appendix C for the early time non-exponential decay effect observed in the X-123 data.

7.1. Epoxy seal

A reduction of the 14.4 keV gamma and Fe K_α and K_β X-ray intensity would occur if there were a continuous loss of Co-57 from the evaporated region. The epoxy seal was examined following the experiment, and showed no obvious signs of degradation; however, some discoloration is evident (see Fig. 24). No radioactivity was found on collection paper at the bottom of the experiment after the run.

7.2. Amptek X-123 detector operation

The first hypothesis considered was the possibility that the X-123 detector was functioning improperly in some way, perhaps losing counts over time. The Co-57 source strength used is well within the operating range of the detector, so we do not expect to see saturation effects. Measurements made in subsequent experiments with the X-123 detector, and also with other detectors, have shown similar non-exponential decay effects, and control experiments have shown exponential decay as expected.

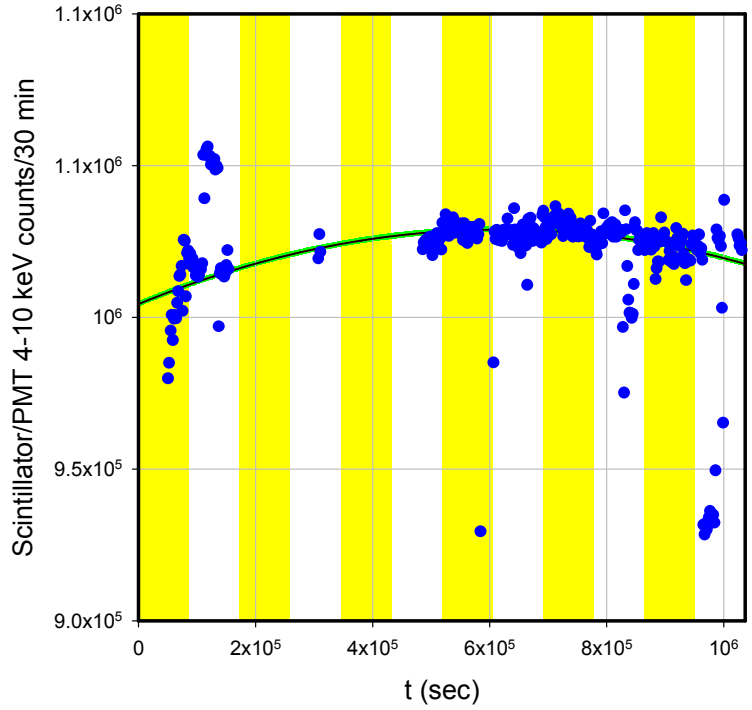

Figure 20. Time history of the of the 4–10 keV channel of the scintillator/PMT detector (*blue circles*); simple parabolic model (*red*); the $\pm 1\sigma$ error bars determined by the square root of the average number of counts (*light green solid region*). The bottom time axis is in seconds; the alternating yellow and white background show the duration of each day between 5/20 and 5/31.

The Sn K_α in this experiment provides for a control – albeit an imperfect one – in that the time history is consistent with exponential decay with the known half-life of 271.74 days to within 1% or so over the length of the experiment. This suggests that during the experiment the detector is able to see time histories which are both exponential at the 1% level, and also non-exponential with enhanced emission at the 17% and 19% level.

Note that in the future we would like to have in the data a time history for a control line, where there is no question as to what the time history should be. One possibility is to field a radioactive source other than Co-57 that would provide a line within the Amptek X-123 detector window. One possibility for this is Sm-151 (90 years half-life), which decays to an excited state in Eu-151 at 21.541 keV that emits a corresponding 21.5 keV gamma that we can see. Another possibility is to make use of another, untreated Co-57 source to photoionize a K-shell (for example in Mo or Pd) to produce a characteristic X-ray in our window. We would want to block such a secondary Co-57 source from the detector to prevent overlap with the treated Co-57 source. The advantage of this approach is that we would then have a control line with a 271.74 day half-life.

It might be that the observed non-exponential decay is associated with lines that have a high count rate. Arguing against this is the non-exponential decay seen in the much weaker Fe K_α escape peak. In future experiments it would make sense to include a proxy for the Fe K_α (such as Ti) and for the 14.4 keV gamma (such as Br), where the K_α would

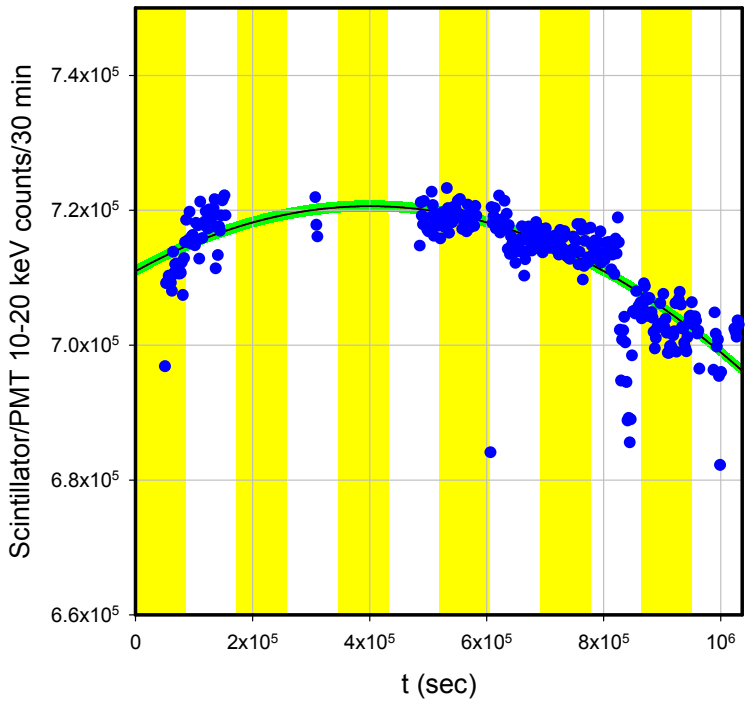

Figure 21. Time history of the of the 10–20 keV channel of the scintillator/PMT detector (*blue circles*); simple parabolic model (*red*); the $\pm 1\sigma$ error bars determined by the square root of the average number of counts (*light green solid region*). The bottom time axis is in seconds; the alternating yellow and white background show the duration of each day between 5/20 and 5/31.

be produced following photoionization from the strong lines resulting in an independent witness to non-exponential decay.

7.3. Relative motion

Since we are using a protective mesh between the sample and X-123 detector, it is possible for relative motion to produce a change in the absorption (which might lead to either an increase or a decrease in the observed X-ray emission).

Arguing against this is the fact that the X-123 was secured by a sample holder, and the sample and wood blocks rested on a stable rack. A substantial force (not present in the experiment) would be required to move the detector, and a significant force (also not present in the experiment) would have been needed to move the sample. It may be that the steel plate moves some when the transducer is powered. Nevertheless one would not expect a smooth exponential relaxation to appear in the signal as was observed in the experiment. Note that the Geiger counter is on the back side with no partial blocking by the aluminum mesh, and we see a similar non-exponential decay effect.

In future experiments it would seem to be prudent to pay direct attention to the relative motion, and also to monitor it with a camera and a microscope to measure whether significant motion occurs.

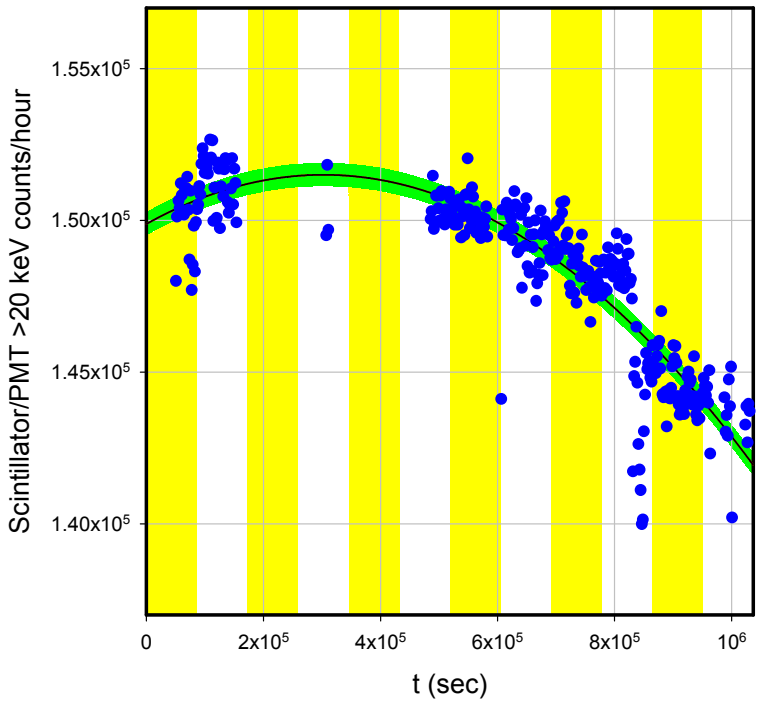

Figure 22. Time history of the of the channels above 20 keV channel of the scintillator/PMT detector (*blue circles*); simple parabolic model (*red*); the $\pm 1\sigma$ error bars determined by the square root of the average number of counts (*light green solid region*). The bottom time axis is in seconds; the alternating yellow and white background show the duration of each day between 5/20 and 5/31.

7.4. Co-57 decay is not accelerated

Other researchers have put forth claims previously for the anomalous accelerated loss of radioactivity in other kinds of experiments (see [51–56]; note that these references represent only a subset of such papers and that there are additional papers in the literature that suggest the existence of such an effect). In part because of this, we entertained the possibility that a loss of activity might be occurring in the May 20 experiment.

Arguing against this is the observed Sn K_α signal with a time history consistent with exponential decay at the 1% level, given the radioactivity present at the beginning of the experiment. This line is produced following photoionization of a K-shell electron by the harder 122.1 and 136.5 keV gammas, so it acts as a proxy in this experiment for the angle-averaged time history of the harder gammas. Since the Fe-57 136.5 keV state is fed from the decay of Co-57 following electron capture, we conclude that the beta decay of Co-57 is consistent with the expected exponential decay (with a 271.74 days half-life) at roughly a level of 1% during the time of the experiment.

An independent argument can be made based on the fact that we would expect the ratio of the intensity of the 14.4 keV gamma line to the Fe K_α line to be constant if produced by a varying beta decay rate. In Fig. 25 we show the ratio of 14.4 keV gamma counts to Fe K_α X-ray counts as a function of time, where a minor decrease in the ratio during the course of the experiment can be seen. This is inconsistent with a loss of Co-57 activity as an explanation

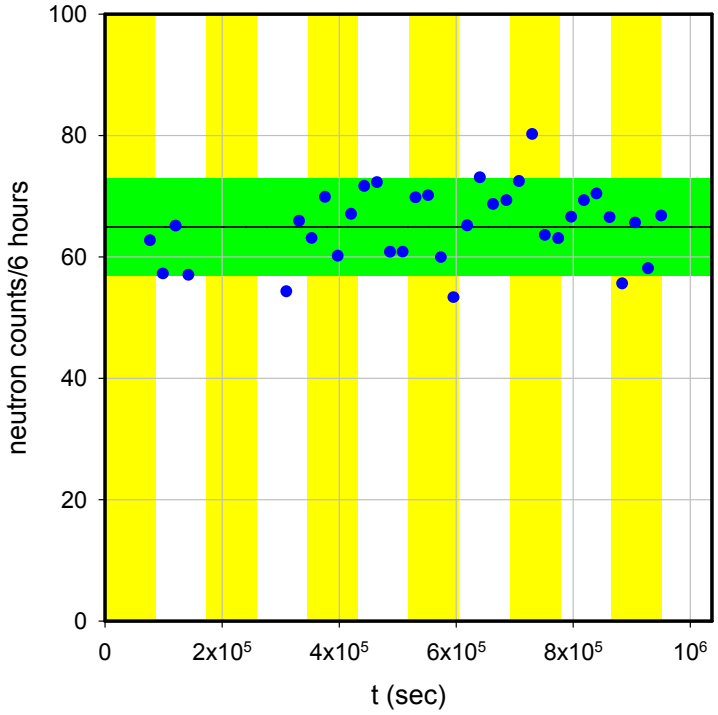

Figure 23. Time history of the neutron counts (*blue circles*); average count rate (*black*); $\pm 1\sigma$ error bars determined by the square root of the average number of counts (*light green solid region*). The bottom time axis is in seconds; the days are marked on top, with the alternating yellow and white background giving the duration of each day.

for the effect.

We interpret the anomalous time-dependence of the emission of the 14.4 keV gamma, and Fe K_α and K_β X-rays as due to an increase in emission at early times, and not due to accelerated decay of Co-57. In subsequent experiments we have observed the emission to increase (weakly) in response to vibrational stimulation, and also in experiments with in situ mechanical stress generated via heat pulses.

7.5. Possibility of up-conversion of 2.21 MHz vibrations

One of the original goals of this experimental effort was to determine whether MHz vibrations can be up-converted to produce nuclear excitation. As discussed briefly above, our results from the May 20 experiments do not support this initial prediction as an explanation for the anomalous observations made (see Fig. 8). In subsequent experiments we have also not seen a prompt response of the X-ray or gamma emission in the Amptek X-123 spectra due to changes in the transducer power.

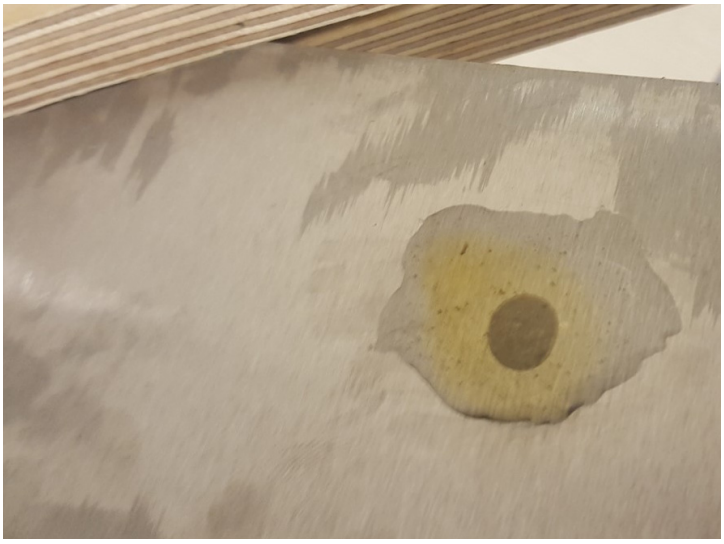

Figure 24. Photograph of the epoxy covering the HCL and Co-57 taken after the May 20 experiment.

7.6. Impact of 2.21 MHz vibrations on the anomaly

The enhanced gamma and X-ray signals were present from the start of the experiment, which from later experimentation we attribute to having been a result of the tightening of the bolts on the wooden clamps and the resulting mechanical stress. However, it could be asked whether the 2.21 MHz vibrations we imposed had any effect, even if not prompt. To shed light on this, we show in Fig. 26 the Fe K_α signal plotted along with the peak transducer power (with a 20% duty cycle the average power is less by a factor of 5). The emission strength does not seem to increase or decrease much while the transducer is run. During the experiment we noticed a weak response (increase) of the photon emission registered by the detector following some of the transducer pulses, which led us to adopt a lower power drive protocol in case the transducer current was impacting the detectors.

7.7. Cause and effect

In the May 20 experiment, the front-side enhancement of photon emission is present from the start of the experiment, and we only observed the subsequent decay (but not the increase preceding it). It was not obvious at the time of the experiment what caused such an enhancement. We assumed initially that something in the protocol used prior to data collection was responsible, with a focus on tightening the bolts on the wood and sample as perhaps key. In later experiments we found that the enhancement can be produced by tightening clamps, or by applying stress in other configurations, as will be described in future publications. Also, triggering the enhancement and the following decay is evident in experiments in which thermal pulses were used to create mechanical stress in situ, as will be discussed in a following paper.

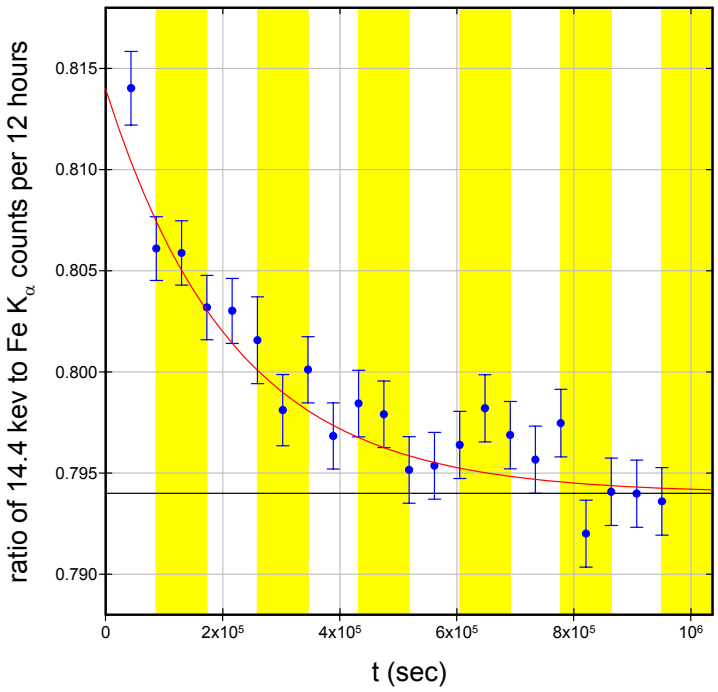

Figure 25. Ratio of counts per 12 h for the 14.4 keV gamma to the counts per 12 h for the Fe K_α X-ray (*blue circles*); simple $a + b\exp(-t/\tau_0)$ fit with $\tau_0 = 2.18 \times 10^5$ s; constant a (*black line*). The bottom time axis is in seconds; the days are marked on top, with the alternating yellow and white background giving the duration of each day.

8. Discussion and Conclusions

The original goal of the runs that now make up the May 20 experiment was to test for excitation transfer of the Fe-57 14.4 keV excited state mediated by strong, piezoelectrically induced vibrations near 2.21 MHz through a (time-correlated) reduction in the 14.4 keV gamma near the source, or an increase from elsewhere in the sample. As discussed above, we saw no evidence for this kind of excitation transfer effect under the conditions of the experiment.

Instead, we saw a different effect. The data shows an enhancement early in the experiment of the 14.4 keV gamma emission, and in the Fe K_α and K_β X-ray emission. This effect can be seen clearly in the data presented above (see Figs. 12, 14 and 15), and was observed with good signal to noise ratio.

Since exponential decay would normally be expected from a radioactive source, the non-exponential decay effect that we saw is anomalous in the sense of being unexpected. As such, the May 20 experiment is in our view potentially an important one.

The May 20 experiment was our first attempt at this kind of excitation transfer experiment. Because of this, we are motivated to consider reproducibility and the possibility of an artifact as issues. The enhancement at early time of

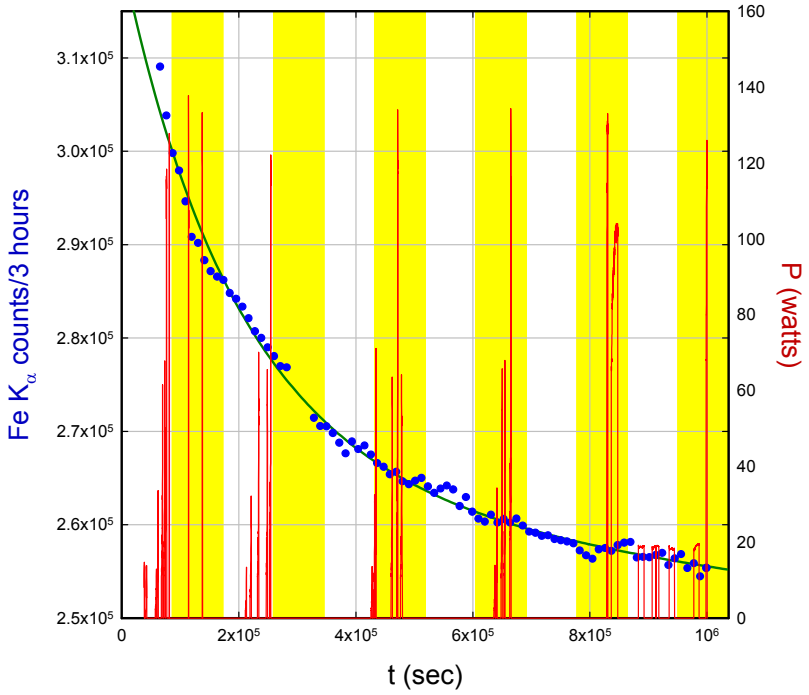

Figure 26. Time history of the Fe K_α signal (*blue circles*); empirical model (*solid green line*); peak transducer power (*solid red line*).

the strong gamma and X-ray lines is reproducible in our experiments, but subsequent observations so far have shown a weaker version of the effect. This indicates that there have been elements of the experiment not under our control (otherwise we would be able to see a large version of the signal each time), and not everything that is important experimentally was fully understood.

The interpretation of the data presents its own set of issues. During the long delay associated with the review process of this paper, there have been many subsequent experiments; and from these experiments some degree of understanding has begun to emerge.

For the early time enhancement of the Fe-57 14.4 keV gamma, and the Fe K_α and K_β X-ray emission, one candidate interpretation involves a small degree of delocalization of the excitation among the Fe-57 nuclei in the substrate evaporated with the Co-57. With the Amptek detector being partially blocked by the protective mesh, it may be that even a small amount of delocalization of the excitation across the substrate provides for a substantial increase (or decrease) of the signal registered by the detector when excitation transfer occurs. This interpretation is discussed further in Appendix C.

Delocalization in connection with this hypothesis would require phonon exchange, and theory indicates that the rate for excitation transfer is much higher for THz phonons. So, this motivates us to think about what the source of these THz phonons might be. The enhancement in the Amptek signal appears (from subsequent experiments) to be correlated to the tightening of the bolts which apply stress to the steel plate through the wood clamps. The long (several

days) duration of the effect motivates us to consider creep, which is the (plastic) deformation/relaxation of a stressed viscoelastic medium. In the case of steel, creep occurs in part through the movement of dislocations, and we expect a substantial population of dislocations in the rolled steel used in the plate on which the Co-57 is deposited. Linear dislocations experience a force in a shear stress field, which in the presence of friction results in an average dislocation velocity (with constant stress). Part of the friction is due to phonon scattering and phonon radiation, which provides a possible mechanism for THz phonon generation and for a non-isotropic THz phonon distribution. This hypothesis is the subject of Appendix D.

The interpretation of the Geiger counter signal involves different spectral lines and a different mechanism. The Geiger counter responds more strongly to the harder 122 and 136 keV gammas than to the 14.4 keV gamma or Fe K_α and K_β X-rays (and we have observed this in subsequent experiments). The Geiger counter looks at the back side of the sample (the Co-57 is on the front side), so that there is no contribution from the 14.4 keV line (which is absorbed completely by the steel plate). There are weak Fe K_α and K_β signals on the back side as a result of photoionization by the harder gammas. Consequently, the Geiger counter time history is dominated by the 122 keV and 136 keV signals in the general vicinity of the Geiger counter, which is over a corner of the plate far from the Co-57 source. In this case, the intensity of these harder gammas at the Geiger counter position is enhanced at early time, and one interpretation for this is an anisotropic distribution of the harder gammas as a result of excitation transfer. This is consistent with early time non-exponential decay seen in later experiments with a NaI detector.

The reduction at early time in the higher channels of the scintillator/PMT detector is thought to be a result of an anisotropy of the harder gammas as well. Instead of being more intense at early time, one interpretation is that the harder gammas in the vicinity of the scintillator/PMT detector, which the detector probably responds to indirectly, is reduced at early time. The time history of the lowest channel is not consistent with this and remains not understood at present.

Our results are generally supportive of the observation of collimated X-ray emission reported previously by Karabut; and also by Kornilova and coworkers.

Our results are also (weakly) supportive of the observations of neutrons and alphas in the experiments of Cardone and coworkers, which we might expect to show up in our experiments if higher stress levels are achieved (assuming that greater stress produces a transfer of higher energy quanta). In a similar way our results are (weakly) supportive of the observations of neutron and alpha emission in the fracture experiments of Carpinteri and coworkers [57–59].

A modification of the time history of a gamma line produced by applying stress to a metal has deep and important theoretical implications. Our candidate interpretations at present involve excitation transfer, mediated by phonon–nuclear coupling. If the experimental results are not artifactual, one is tempted to conclude that phonon–nuclear coupling occurs and can be studied experimentally.

One goal of our research is to develop a well defined and well characterized version of the experiment, which would be appropriate to share with others. The May 20 experiment described here is the first version of an excitation transfer test and is followed by subsequent experiments which we will report on in future publications.

Appendix A. Review of Phonon Exchange and Related Mechanisms

The May 20 experiment was carried out in order to provide experimental feedback on a theoretical proposal for an excitation transfer effect. This motivates us to provide here a brief review of phonon–nuclear coupling and excitation transfer. These mechanisms constitute building blocks for proposed up-conversion, down-conversion and subdivision mechanisms, which have been the focus of theoretical work aimed at shedding light on various anomalies in Condensed Matter Nuclear Science. Some discussion of these mechanisms follows in this Appendix.

Appendix A.1. phonon–nuclear interaction

We can write the phonon–nuclear interaction for a single nucleus in the form [5]

$$\hat{H}_{int} \;=\; \hat{\mathbf{a}} \cdot c\hat{\mathbf{P}}, \tag{A.1}$$

where $\hat{\mathbf{a}}$ operates on the internal nuclear degrees of freedom, and where $\hat{\mathbf{P}}$ is the momentum of the nuclear center of mass which depends on the vibrations. We can think of the $\hat{\mathbf{a}}$ operator as causing an internal nuclear transition, and the momentum operator $\hat{\mathbf{P}}$ as either creating or destroying a phonon. If dealing with two specific nuclear states and one highly excited phonon mode it is possible to reduce the interaction to

$$\hat{H}_{\text{int}} \;\rightarrow\; V_0(\hat{c}^{\dagger} + \hat{c})\Big(\mid \uparrow\rangle\langle\downarrow \mid + \mid \downarrow\rangle\langle\uparrow \mid \Big), \tag{A.2}$$

where $\hat{c}^{\dagger}$ and $\hat{c}$ are phonon creation and annihilation operators, and where $\mid \uparrow\rangle\langle\downarrow \mid$ raises the internal nuclear state $\mid \downarrow\rangle\langle\uparrow \mid$ lowers it. For dynamics governed by this kind of interaction, a single phonon exchange (absorption or emission) is coupled with a nuclear transition (raising or lowering).

The coupling of atoms and nuclei with the electromagnetic field is mediated by a similar interaction Hamiltonian, so it would be natural for us to think of a nuclear transition decay associated with phonon emission in connection with this Hamiltonian. While people do study single phonon exchange in connection with nuclear spin splitting in a strong magnetic field, here we are interested in internal nuclear states with energies that differ by keV or more, in which case there is no possibility of nuclear excitation or decay through the exchange of a single phonon. Instead we need to consider higher-order processes in which two or more phonons are exchanged.

Appendix A.2. Excitation transfer

The simplest higher-order process relevant to the discussion is excitation transfer. In the simplest case where two identical nuclei interact with a common excited vibration mode, it is possible to transfer nuclear excitation from one nucleus to the other. Suppose that nucleus A is excited while nucleus B is in the ground state initially. Then the exchange of one phonon can cause nucleus A to de-excite to the ground state, resulting in an (off-resonant) intermediate state where both nuclei are in the ground state. And then the exchange of a second phonon can cause nucleus B undergo a transition to the excited state. If the number of phonons is the same afterward as before, then this excitation transfer process can be resonant. The different pathways possible at lowest order are shown in Fig. 27.

This kind of excitation transfer process is the lowest-order effect that we might hope to see in the experiment (since it involves the exchange of only two phonons). Resonant excitation transfer can produce phase coherence if order is present, which can result in the angular anisotropy thought to be responsible for non-exponential decay effects associated with the harder gammas in the May 20 experiment.

Collimated gamma emission is possible in the case that phase coherence is present over a larger area of the surface, and where the lattice planes are aligned [60]. We had previously considered the presence of collimated X-rays to signify the presence of phonon up-conversion with a uniform vibrational mode. This should be updated to include (as more likely) the presence of resonant excitation transfer at the surface.

Resonant excitation transfer can move excitation from one location to another. In the event that the phonon mode is delocalized, such as for piezoelectrically induced MHz vibrations corresponding to plate resonances, the excitation has the possibility of being transferred from the vicinity of the radioactive source to pretty much anywhere in the plate. This is the effect predicted in the original design of the experiment. In contrast, a single excitation transfer event mediated by high frequency vibrations in the GHz or THz regime will only move the excitation a small distance, since

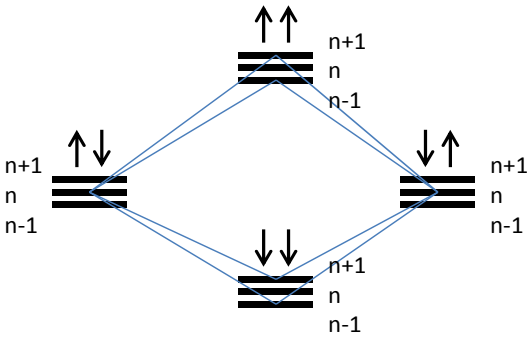

Figure 27. Simplified schematic of excitation transfer between two nuclei with single phonon exchange. The ↑ represents a nucleus in an excited state, and the ↓ represents a nucleus in the ground state.

these modes are very lossy and hence localized. However, many sequential excitation transfers with high frequency vibrations has the potential to lead to an overall transfer to a remote location.

The phonon–nuclear coupling interaction within the discussion above involves E1 symmetry (with only a single phonon exchange associated with each nuclear transition), while the transition from the Fe-57 ground state to the 14.4 keV excited state has M1+E2 symmetry. Consequently, excitation or de-excitation would involve two-phonon exchange and transitions to intermediate states, with excitation transfer involving the exchange of $0,\pm2,\pm4$ phonons.

Appendix A.3. Up-conversion

As discussed above our interest in up-conversion comes from an interest in the down-conversion mechanism conjectured to be the explanation for the absence of commensurate nuclear radiation associated with excess heat in the Fleischmann–Pons experiment. Models that we have studied for down-conversion also describe up-conversion on equal footing [61–64].

From the simplest perspective in the up-conversion process under consideration a great many phonons are exchanged to produce nuclear excitation (Fig. 28). These models indicate that up-conversion places more constraints on the requirements for the physical system than excitation transfer, with the most severe requirements coming when the number of quanta up-converted Δn

$$\Delta n \;=\; \frac{\Delta E}{\hbar\omega_0} \tag{A.3}$$

is large. Here ΔE is the up-converted energy and $\hbar\omega_0$ is the phonon energy. This consideration favors high frequency phonons in the THz regime. Up-conversion with 2.2 MHz phonons is particularly difficult since the associated phonon energy is very small (9.1 neV). The highest frequency phonons for BCC crystalline iron are near 38 meV [65], which according to the models makes up-conversion to the keV regime much more accessible. Our preference in all cases is to work with higher frequency THz phonons. However, in our initial experimental work, we focused on MHz vibrations in part since the experiments were much easier to be implemented, and since previous experimental work suggested that positive results could be obtained with lower frequency stimulation.

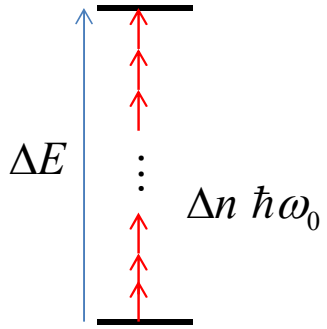

Figure 28. Simplified schematic of up-conversion for nuclear excitation by the conversion of a large number of phonons.

Up-conversion in the models occurs through the energy exchange of a great many single-phonon exchange interactions taking place rapidly before decoherence occurs. Excitation transfer effects might be observable under conditions where only a few phonon exchange interactions occur; however if up-conversion is observed then we know that a very large number of phonon exchange interactions must have occurred.

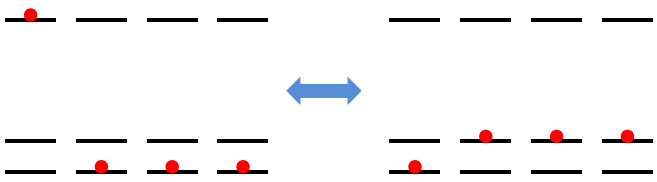

Figure 29. Simplified schematic of subdivision, where a single highly excited nuclear state is exchanged for many nuclear excitations at lower energy.

Appendix A.4. Subdivision

A problem was found when we made use of down-conversion models to reduce the large 24 MeV ΔE value associated with the $D_2/^4He$ transition for excess heat in the Fleischmann–Pons experiment, where Δn is very large (on the order of 10^9 or greater), and it seemed difficult to connect theory with experiment. However, if the large 24 MeV quanta is instead exchanged for many lower energy (keV-level) nuclear excitations, then the resulting down-conversion problem becomes much more attractive. This conversion of a high energy nuclear excitation into many smaller nuclear excitations was termed "subdivision" (see Fig. 29), and it requires a modest number of phonon exchange interactions to occur. Typically there will not be a precise resonance available, so the energy mismatch δE will need to be taken up through down-conversion

$$\begin{aligned} \Delta E_1 &= \Delta N \Delta E_0 + \delta E \\ &= \Delta N \Delta E_0 + \Delta n \hbar \omega_0. \end{aligned} \tag{A.4}$$

A hindrance of the reaction rate can come from either too many excitations ΔN, or more likely from too many up-converted phonons Δn.

Appendix B. X-123 Calibration

The analysis of the data for the May 20 experiment depends in an important way on the calibration of the X-123, which motivates us to consider the calibration briefly in this appendix.

Appendix B.1. Calibration

For calibration, we chose the three strongest lines which result directly from the Co-57 source (the Fe-57 14.4 keV gamma, and the Fe K_α and K_β X-rays), along with two much weaker but clear X-ray lines (the Sn K_α and the Sb K_α). These are listed in Table 1. For the May 20 data set, we summed all available spectral data for the 11 days of the run to a single cumulative spectrum, and used a local Gaussian fit with a sloped baseline

$$f(i) = A \exp\left\{ -\frac{(i - i_0)^2}{\Delta i^2} \right\} + B + Ci \tag{B.1}$$

over channels in the vicinity of the lines, where i is the channel number, and where the other parameters (A, i_0, Δi, B, C) are determined by least squares fitting.

The Amptek X-123 detector settings were not changed after the experiment, and we might expect a minor drift over the following months. Channel averages are given in Table 1 for the May 20 spectra, and also for a spectrum taken subsequently starting on August 6, 2017. There are only minor differences in the average channel values; however, the

Table 1. Major lines chosen for determination of the calibration parameters.

Line	Energy (eV)	Average channel May 20, 2017	Average channel Aug 6, 2017	FWHM (eV)
Fe K_α	6399.5	490.931	490.795	173.4
Fe K_β	7058.0	540.569	540.405	182.7
Fe-57 γ	14421.9	1099.713	1099.394	222.1
Sn K_α	25192.6	1919.218	1918.422	408.9
Sb K_α	26272.0	2002.277	2000.738	381.1

spectra are sufficiently close that it is possible to make use of calibration spectra taken subsequently to help with the line identifications.

Appendix B.2. Linear calibration

We used least squares fitting for the May 20 data set to develop a linear calibration of the form

$$E(\mathrm{eV}) \;=\; a_0 + a_1 i, \tag{B.2}$$

where E is the energy in eV, and where i is the channel number; with fitting parameters given by

$$a_0 \;=\; -\,50.2842, \qquad a_1 \;=\; 13.1504. \tag{B.3}$$

The standard deviation associated with this fit is

$$\sigma \;=\; 8.937\,\mathrm{eV}. \tag{B.4}$$

Appendix B.3. Cubic calibration

Least squares fitting was also used to develop a cubic calibration for the May 20 data set with a lower standard deviation based on

$$E(\mathrm{eV}) \;=\; a_0 + a_1 i + a_3 i^3 \tag{B.5}$$

with fitting parameters

$$a_0 \;=\; -\,75.413, \qquad a_1 \;=\; 13.1943, \qquad a_3 \;=\; -\,8.39972 \times 10^{-9}. \tag{B.6}$$

The standard deviation in this case is

$$\sigma \;=\; 4.801\,\mathrm{eV}. \tag{B.7}$$

This cubic calibration does a little better than a quadratic calibration, for which the standard deviation is 5.122.

Appendix B.4. Peak identifications

Results for the May 20 spectra augmented with calibration runs carried out in August are summarized in Table 2. We see good agreement between known line positions and estimates for the two calibrations. During the runs in August we took XRF calibration spectra in place with Ti, Zn and Sn samples, which confirmed earlier identifications in the case of Zn and Sn. The Ca K_α and K_β lines were much stronger in the August spectra.

We were not expecting to see escape peaks with a Si-PIN detector since the fluorescence yield of the Si K_α is low; however, there are clear escape peaks present associated with the strong Fe-57 gamma and Fe K_α and K_β lines at an energy of

$$E[\mathrm{escape}] \;=\; E_0 - E[\mathrm{Si\ K}_\alpha] \;=\; E_0 - 1739.8\,\mathrm{eV}. \tag{B.8}$$

Identifications for the weaker lines in the summed spectra for the May 20 experiment listed in Table 2 are shown in Fig. 30.

Table 2. Average channel numbers for identified and also for unidentified lines from the May 20 data; average channel numbers for lines observed in August runs are in brackets; known energies for the different X-ray transitions and gamma transition are listed, along with energy values from the linear and cubic fits.

Line	Average channel	Energy (eV)	Linear energy (eV)	Cubic energy (eV)
Ca K_α	[284.999]	3690.5	3697.6	3684.8
Ca K_β	[309.090]	4012.7	4014.4	4002.6
Ti K_α	[347.324]	4508.8	4517.2	4506.9
Ti K_β	[378.609]	4931.8	4928.6	4919.6
Fe K_α escape	358.040	4659.5	4658.1	4648.3
Fe K_β escape	408.683	5318.0	5324.1	5316.3
Fe K_α	490.931	6399.5	6405.7	6401.1
Fe K_β	540.569	7058.0	7058.4	7055.7
Zn K_α	[660.381]	8631.1	8634.0	8635.4
?	688.133		8998.9	9001.3
Zn K_β	[732.641]	9572.0	9584.2	9588.0
?	740.924		9693.2	9697.1
Fe-57 γ escape	967.691	12681.9	12675.2	12685.0
Fe-57 γ	1099.713	14421.9	14411.4	14423.4
Zr K_α	1198.711	15746.3	15713.2	15726.3
Ag K_α	1683.961	22103.1	22094.5	22103.2
Sn K_α	1919.218	25192.6	25188.2	25187.9
Sb K_α	2002.277	26272.0	26280.5	26275.8

Appendix B.5. Unidentified peaks at 9.00 and 9.69 keV

There are two weak lines present in the May 20 spectra with energies of 8998.9 and 9693.2 eV based on the linear calibration which have been frustrating to identify. We had initially (prior to the research leading to an accurate calibration) thought that they were Zn K_α and K_β lines; however, in the August spectra we can see the 8998.9 eV line offset from the Zn K_α and K_β. Certainly there are X-ray transitions known near 9.00 keV; in the NIST data base there are Cu KM and KN lines between 8.977 and 8.980 keV, and Hg and Hf LM lines between 9.019 and 9.023 keV, none of which are attractive candidates. Around 9.69 keV there are also lines known; there is a W LM line near 9.673 keV, Tl and Au LM lines listed between 9.701 and 9.713 keV, and Ta and W LN lines predicted between 9.708 and 9.717 keV, none of which are compelling candidates. In all cases one would expect to see other lines with appropriate relative intensities; however, and these other lines are not present in the spectra. We took data with a Ta foil irradiated by Co-57, and the emission pattern looks nothing like the unidentified spectral features.

We considered the possibility that the unidentified lines might be summation peaks according to

$$E[\mathrm{Fe\ K}_\alpha + \mathrm{Cl\ K}_\alpha] \;=\; E[\mathrm{Fe\ K}_\alpha] + E[\mathrm{Cl\ K}_\alpha] \;=\; 6399.47 + 2621.87 \;=\; 9021.33\,\mathrm{eV}, \tag{B.9}$$

$$E[\mathrm{Fe\ K}_\beta + \mathrm{Cl\ K}_\alpha] \;=\; E[\mathrm{Fe\ K}_\beta] + E[\mathrm{Cl\ K}_\alpha] \;=\; 7057.98 + 2621.87 \;=\; 9679.85\,\mathrm{eV}. \tag{B.10}$$

Since the HCl volatilizes during the evaporation of the $^{57}CoCl_2$ in 0.1 M HCl solution on the surface of the steel, we would not expect much chlorine to be present on the surface in amounts more than twice the Co-57. In spectroscopy measurements we do not see a clear Cl K_α line in the Amptek X-123 spectrum, due in part to the high background in the low energy channels, and in part to the weakness of the signal.

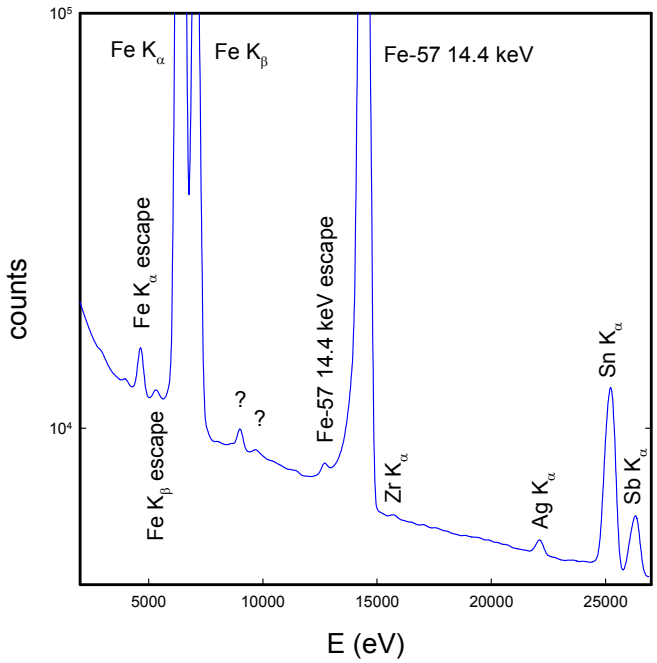

Figure 30. Weak lines in the smoothed time-integrated spectrum for all data from the May 20 experiment including identifications.

We carried out an experiment with graphite sheets to block the low energy lines while passing the Fe K_α in order to clarify the issue. The result was that the 9.00 keV line was not eliminated, which rules out the possibility of the unidentified lines being summation peaks.

One speculative possibility for the 9.00 keV line identification is that it might be an escape peak associated with the 14.4 keV gamma due to a low-level impurity in the Si. We can compute for a Cr impurity

$$E[^{57}\mathrm{Fe}\ 14.4219\ \mathrm{keV}] - E[\mathrm{Cr}\ \mathrm{K}_\alpha]\ =\ 9.007\ \mathrm{keV}. \tag{B.11}$$

This is in good agreement with the observed linear near 9.00 keV.

Appendix B.6. Time-history of the 9.00 keV line

The time history of the 9.00 keV line is non-exponential (see Fig. 31), but shows only a modest version of the early time enhancement (a roughly 2% increase, where we might have expected to see a roughly 20%). This is explainable if only the weak line itself is showing a strong non-exponential decay, with the background decaying much more slowly consistent with the 271.74 day half life. To clarify this it would be useful to separate out the time dependence of the local background from the line itself, which is problematic since the line is weak which leads to statistical issues. Perhaps the most straightforward way to see the relative contributions in this case is to look at the contour plot of

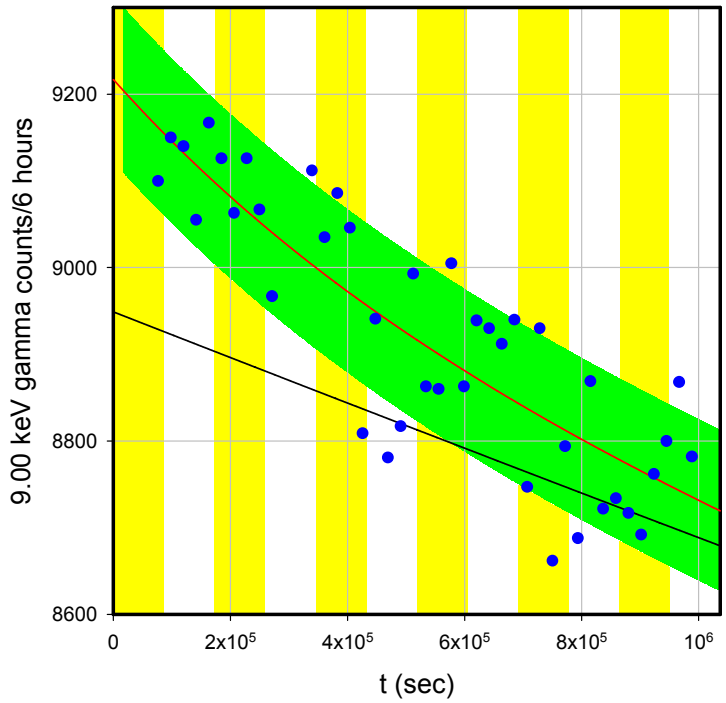

Figure 31. Time history of the of the unidentified 9.00 keV peak (*blue circles*); empirical model (*red*); exponential decay with 271.74 days half-life consistent with empirical model (*black*); the $\pm 1\sigma$ error bars determined by the square root of the average number of counts (light green solid region). The bottom time axis is in seconds; the alternating yellow and white background show the duration of each day between 5/20 and 5/31.

counts per 6 h as a function of time and energy (shown in Fig. 32). We see that the background away from the line is reasonably constant in time, while the line itself shows a noticeable decrease over the duration of the experiment.

Appendix C. Possibility of a Delocalization Effect

Although the May 20 experiment shows an unexpected non-exponential decay effect, the experiment itself does not provide direct information as to how such an effect is produced. In Appendix A, we reviewed briefly some of the effects that we might have predicted to see, but in retrospect our focus has to be on such excitation transfer effects which require the least amount of new physics to give effects in an experiment. As a weak effect, excitation transfer would be expected to be dominated by a resonant version of the effect (in which no net energy is exchanged with phonons), which would produce phase coherence. Phase coherence is potentially observable via dynamic angular anisotropy, which in the May 20 experiment is most likely the reason that we see non-exponential time histories in the Geiger counter (which responds most strongly to the 122 and 136 keV gammas), and perhaps in the scintillator/PMT detector as well.

If the indirect coupling matrix element associated with excitation transfer is strong, then we would expect many excitation transfers to be possible before dephasing occurs, and also that non-resonant excitation transfer events would

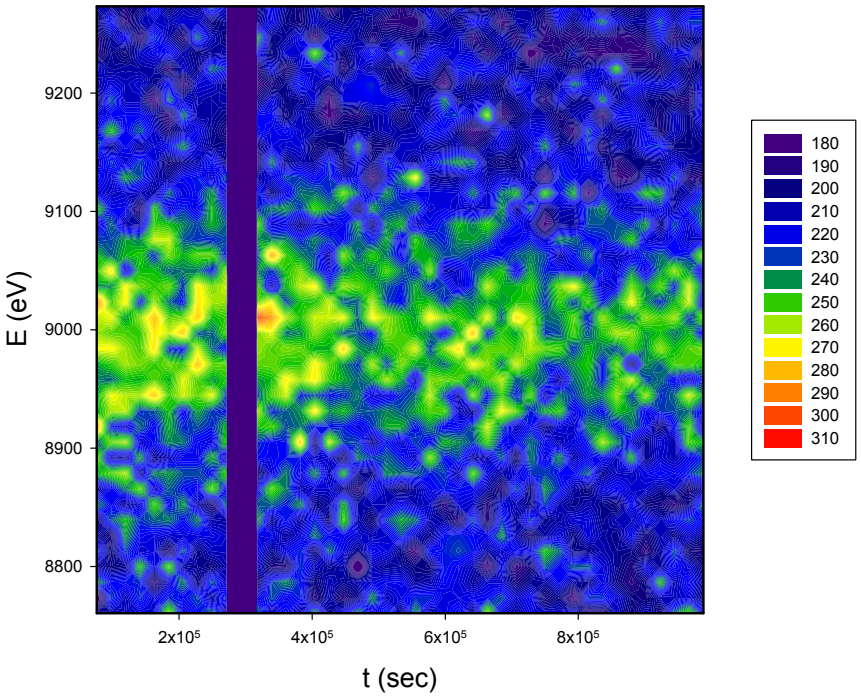

Figure 32. Time history (counts per 6 h) of the spectrum of the unidentified 9.00 keV peak; the time axis (*bottom*) is in seconds; the energy is on the left.

dominate. Due to this latter effect we would not expect phase coherence, which would suggest a lack of angular anisotropy associated with the 14.4 keV gamma. Since the Fe K_α X-ray results from incoherent decay processes, we would not expect to see angular anisotropy effects associated with the strong X-ray transitions. These various theoretical statements appear to be consistent generally with results from the May 20 experiment, and also from subsequent experiments. One might have argued that the non-exponential decay effect in the 14.4 keV gamma was due to angular anisotropy, but in such a scenario the explanation of a very similar non-exponential decay effect in the Fe K_α and K_β X-rays becomes problematic.

The notion of multiple excitation transfers occurring prior to the decay of the 14.4 keV excited state is conceptually straightforward. In an abstract sense we understand that multiple excitation transfers will produce a larger delocalization of excitation in the strong coupling regime compared to the weak coupling regime. We then run into issues associated with the suggestion that enough excitation transfers can occur within the 98.3 ns half-life of the 14.4 keV state to produce delocalization at the hundred micron to millimeter scale, which is what would be required to account for non-exponential time histories observed by the X-123 detector with the coarse aluminum mesh. For example, if excitation transfer were mediated by THz phonon exchange, then we would expect the separation between nuclei for a single excitation transfer to be restricted to on the order of 100 Å. Unless this fast excitation transfer effect were directional, it is hard to imagine that enough isotropic excitation transfer events could move an excitation more than 100 μm across the plate surface.

There are other issues as well. We had evaporated the Co-57 onto a steel plate, in part because the steel has Fe-57 as a constituent at the level of 2.11%. If excitation transfer can delocalize excitation more than 100 μm, then we might expect the excitation to go into the steel, where the emitted low energy radiation would be absorbed. On the face of it, excitation transfer consistent with this picture can lead to a non-exponential effect in which the emission registered above the plate surface is reduced instead of increased.

At this point we take advantage of many subsequent months of thought and contributions from colleagues in order to devise a relevant picture.

The evaporation of a sessile droplet on a flat surface has recently become a topic of interest, as reviewed in Ref. [66]. We are familiar with rings left following the evaporation of coffee, which itself has been studied in some detail (see e.g. [67]. One would expect a similar model to apply for a non-colloidal liquid. Salt crystal formation on various flat insulators was studied in Ref. [68], while the evaporation of various salts on a metal surface was studied in Ref. [69]. We have so far not found studies of the evaporation of $CoCl_2$ in aqueous HCl on steel, but we would expect (and by now have observed) a ring resulting from our evaporation. The ring formed during the evaporation of the solution is a bit larger than 1 cm in diameter, with a width of roughly 0.5 mm.

The amount of radioactive chloride that corresponds to the initial activity is small, and by itself would not constitute enough material to be observable as a ring (as observed by Malcolm Fowler/Los Alamos). Consequently, we know that there must be something else in the residue, and the only question is what. An elemental or isotopic analysis of the solution would have been appropriate to settle this, but we were not able to arrange for such an analysis due to the radioactivity, and the remainder of the solution had already been used for a second evaporation before we understood that this was important. From e-mail exchanges with Eckert & Ziegler we understand that probably there is little other than Co-57 present in the stock which they buy from their suppliers. If the stock was made a long time ago, then it is possible that Fe-57 will have accumulated. Since according to Eckert & Ziegler such stock can be several years old, in the picture we are working with at present it is presumed that most of the residue is daughter Fe-57 from earlier Co-57 decays.

If so, then the residue itself will be preferred for receiving excitation transfer (in comparison to the Fe-57 in the steel plate) due to the ready availability of ground state Fe-57, and we might expect excitation transfer to result in excitation moved from one part of the residue to another. We know that the residue is strongly inhomogeneous (because we can see the ring), and we might expect that excitation would go preferentially to where there is more Fe-57.

Suppose now that the coarse aluminum mesh between the plate and the Amptek X-123 detector blocks emission from where the excitation is originally coming from, and passes emission from where the excitation is transferred to. In this picture we might expect a non-exponential enhancement of registered emission. The enhancement can lead to a non-exponential decay effect, as observed, assuming that more phonons are present early on due to relaxation (of moving dislocations, or viscoelasticity in the epoxy, or rearrangement at interfaces – see section below for details). If so, then we might equally well have seen a non-exponential increase (as has been observed in later experiments) if the mesh were to pass emission from where excitation comes from. It would also have been possible to see a small effect (as has been observed), if on average emission is passed equally from regions where excitation originates from and where excitation ends up. This general picture is consistent as far as we know from much later experiments focusing in localized regions within the substrate.

What is left then is to think about the spatial scale and implications. To account for the magnitude of the non-exponential component, excitation transfer on a spatial scale of a few hundred microns to the millimeter scale is needed. How this happens is not understood at present. There are some candidate hypotheses available. One is that the excitation transfer is sufficiently fast that many small 100 Å steps produce effects at the larger scale. Another hypothesis is that the excitation transfer is directional, perhaps as a result of non-resonant phonon exchange, or perhaps as a consequence of the inhomogeneity of the Fe-57. Another possibility is that in the strong coupling limit highly off-resonant states are occupied which have no decay channels open, resulting in a reduction in the overall decay rate.

Appendix C.1. Al mesh

The mesh is thick (absorbing) for the 14 keV gamma (97%) and Fe K_α and K_β X-rays (100%), so that transmission only occurs through the holes. The sensitive part of the Si PIN detector is a square 6 mm^2 in area. We assume for this discussion that the 6 mm^2 area of the detector is located 10 cm below the source. In between the source and detector is the mesh. We know the size of the holes in the mesh (0.47625 cm diameter), and the average transmission (51%).

Suppose we define r to be the radius of the hole, and b to be the distance between the center of a hole and the nearest neighbor. In this case, the average transmission t is the ratio of the area of the holes in one triangle with neighboring hole centers as vertices divided by the area of the triangle

$$t \;=\; \frac{\pi r^2/2}{\sqrt{3}b^2/4}. \tag{C.1}$$

From this we can write the distance between the holes to be

$$b \;=\; \sqrt{\frac{2\pi r^2}{\sqrt{3}t}} \;=\; 0.635\ \text{cm}. \tag{C.2}$$

Appendix C.2. Detector alignment

The Amptek X-123 detector area (6 mm^2) is small compared to the hole area (17.8 mm^2), so that whether the X-ray and gamma ray signals make it through the mesh is dependent on whether there is a hole above the detector or not. In the May 20 experiment there was no attempt at optimization of the signal relative to the local mesh position, so that the position of the detector relative to the hole is unknown. This was an uncontrolled random variable in the early experiments.

Appendix C.3. Count rate and mesh transmission

We can make a rough estimate for the mesh transmission from the observed count rate of the Fe-57 14.4 keV gamma. The expected count rate R can be estimated in terms of the source strength S according to

$$\begin{aligned} R =&\ \Delta\Omega \times T_{\text{mesh}} \times \eta \times S \\ =&\ \left(\frac{6\ \text{mm}^2}{4\pi d^2}\right) \times T_{\text{mesh}} \times \eta \times \left(0.091 \times 200\ \mu\text{Ci} \times 3.7 \times 10^{10}\ \text{Bq}\right) \\ =&\ \left(4.77 \times 10^{-5}\right) \times T_{\text{mesh}} \times \eta \times \left(6.73 \times 10^5\right) \frac{\text{counts}}{\text{s}}, \end{aligned} \tag{C.3}$$

where $\Delta\Omega$ is the acceptance angle, where T_{mesh} is the (unknown) transmission of the mesh, and where η is the efficiency of the detector. According to [45] there are 9.1 14.4 keV gammas produced per 100 Co-57 disintegrations. From the Amptek website the intrinsic efficiency (Be window and Si absorption) of the detector is about

$$\eta \;=\; 0.725. \tag{C.4}$$

The expected count rate is then

$$R \;=\; 23.3\, T_{\text{mesh}}\, \frac{\text{counts}}{\text{s}}. \tag{C.5}$$

The observed count rate in the May 20 experiment for the 14.4 keV gammas is about

$$R \;=\; 4.15 \times 10^5\, \frac{\text{counts}}{6\text{ h}} \;=\; 19.2\, \frac{\text{counts}}{\text{s}}. \tag{C.6}$$

These estimates are consistent with a mesh transmission of

$$T_{\text{mesh}} \;=\; 0.82 \tag{C.7}$$

with substantial uncertainties at this point in the Co-57 activity, and in the distance d between source and detector. The relatively good agreement between source strength and count rate in this estimate is encouraging; however, it is not possible to develop an accurate estimate for the mesh transmission in this case.

A similar computation for the Fe K_α is not so consistent. The source efficiency is more than 5 times higher, so one might expect to see a much higher count rate. Amptek does not report an absolute efficiency for the X-123 Si PIN detector, but lists an intrinsic efficiency near 95%. Including photoabsorption in air helps to a minor degree to explain why we do not see a 4–5$\times$ higher count rate. It is likely that the X-123 has a low absolute efficiency near 6.4 keV. This conclusion is supported by the study of Ref. [70].

Appendix C.4. Discussion

The relative position of the source, mesh and detector are critical parameters which were uncontrolled in the May 20 experiment due to the exploratory nature of this experiment, and which have a big impact on reproducibility. We were not aware of this in the early runs, and as a result there was much variation in the magnitude and sign of the non-exponential decay effect. A consequence of this is that this kind of experiment would be expected to be very sensitive to the relative positions, and changes during the experiment would produce artifacts similar to the effects reported.

The large magnitude of the non-exponential component of the signal in the May 20 experiment indicates delocalization occurring on a spatial scale no less than hundreds of microns, and perhaps more than 1 mm, given the picture outlined above. If so, this would be stunning, and would be an effect well worth studying in detail much further.

Experiments in which Fe-57 (free of Co-57) is placed near the residue are of interest, as we will want to see excitation going into the Fe-57 from regions containing the Co-57 to have confidence that we are seeing this kind of excitation transfer.

Appendix D. Possibility of THz Phonon Generation from Creep

Given the experimental results described above, it is not yet possible to draw any firm conclusions about what is going on in detail in the sample from the data presented. On the other hand, if the enhanced early time emission is real, then it needs an explanation, and we are going to need hypotheses that can be addressed in future experiments and in future theoretical work.

The experiment was set up and run in order to see whether we could induce delocalization of the Fe-57 14.4 keV excited state through phonon exchange by vibrating the steel plate strongly at 2.21 MHz. This did not seem to work as discussed above. The rate for excitation transfer in a molecule in the absence of loss scales as the phonon frequency squared [23], which draws attention to the low 2.21 MHz phonon frequency as an issue, and also focuses attention

on the possibility that THz phonons might be present in the experiment. If so, then we are interested in mechanisms present in the experiment which might generate THz phonons.

Since the early time enhancement was present when we began taking data, our attention is focused on what happened to the sample prior to the experiment. Before the May 20 experiment, the steel plate had been resting on a rack with no wood blocks attached, but with piezoelectric transducer and ultrasonic coupling gel on top, and with earlier sets of transducer pulses applied. In preparation for the experiment the sample was picked up, then one corner was placed between two pieces of wood and bolts tightened, at the equivalent force of about 2000 lbs. This was followed by a similar procedure for the other two pieces of wood. Then the steel plate with wood blocks was placed on the rack as in the photograph (Fig. 3), and data was collected.

Appendix D.1. Ultrasound absorption issues

The stress in the steel is greatest near the wood clamps, with compressional stress between, and shear stress near the edge outside of the steel-wood interface. Phonons generated near the clamps could propagate to the vicinity of the Co-57 substrate only at "low" frequency, since ultrasonic attenuation in steel leads to an absorption length on the order of 1 cm near 10 MHz [71–73]. There is little reason to believe that this will make a difference given that driving the steel plate with over 100 watts near 2.21 MHz does not produce an observable response that can be correlated with the period when the plate is driven.

THz phonons are strongly absorbed in all solids, and we would expect an absorption length on the order of 10 nm or less. This focuses our attention on dislocations, which have a long lifetime, which are present in rolled steel, and which scatter and generate THz phonons locally when they move. THz phonons scattered or radiated then by moving dislocations very close to the nuclear excitation have the potential to produce excitation transfer.

Appendix D.2. Creep and dislocation movement

The early time enhancement of the gamma and X-ray emission seen in the experiment appears to decay away with a relaxation time of about two and a half days. This relaxation time is not connected to the nuclear levels of Fe-57 in an obvious way; however, it may be consistent with creep, since there is the possibility of plastic deformation in the steel [74–77] and wood [78–80]. The plastic deformation associated with creep occurs through the flow of dislocations.

Dislocations experience a force in the presence of stress [81], and plastic deformation in iron is dominated by screw dislocations [82]. The dislocation velocity $v(T)$ increases with temperature [83], in one model according to [84,85]

$$v(T) \;=\; \nu_{\rm D}\frac{b}{l_{\rm c}}\frac{L}{l_{\rm c}}a\exp\left\{\frac{\Delta G(\sigma)}{k_{\rm B}T}\right\}, \tag{D.1}$$

where $\nu_{\rm D}$ is the Debye frequency, b the distance between two rows of atoms in a slip plane, $l_{\rm c}$ the critical length for kink nucleation, L the length of the linear dislocation, where a is the slip distance for a single activation, and where ΔG is the free energy of activation which is a function of stress σ (edge and screw dislocations experience a force under shear stress).

The rate of plastic deformation is given by what is often referred to as Orowan's equation [86–88]

$$\frac{\partial}{\partial t}\epsilon \;=\; \alpha b\rho\overline{v}, \tag{D.2}$$

where ϵ is the strain, b the Burgers vector, ρ the density of dislocations, $\overline{v}$ the average dislocation velocity, and α is a geometrical factor. It would follow from these arguments that we would might expect the temperature dependence of

creep to obey an Arrhenius law. Consistent with this, Cuddy reported that the observed rate of creep in steel could be fit by a model of the form [75]

$$\frac{\partial}{\partial t}\epsilon \;=\; A\sigma_A^n \exp\left\{-\frac{Q}{RT}\right\}, \tag{D.3}$$

where Q is an activation energy, σ_A the applied stress, n a fitting parameter (5.8 for the measurements fitted), and A is a proportionality constant. If THz phonons from plastic deformation are responsible for the effects observed, then we might expect a version of the experiment run with steel at elevated temperature to show a faster decay.

In future experiments we would like to see whether the anomaly is sensitive exclusively to shear stress, or whether tensile or compressional stresses also can produce anomalies. Such tests would be useful for shedding light on how best to design new experiments, as well as being helpful for theory. Late in the writing of this paper an early paper came to our attention describing the observation of gamma radiation emitted as a result of various materials subjected to very high levels of shear stress [89].

Appendix D.3. Time-dependence and creep

The empirical fitting model that we made use for the intensity of the gamma and X-ray emission is consistent with

$$I(t) \;=\; I_0\ \mathrm{e}^{-t/\tau} \exp\left\{b\ \mathrm{e}^{-t/\tau_0}\right\} \;\rightarrow\; I_0\ \mathrm{e}^{-t/\tau}\left[1 + b\ \mathrm{e}^{-t/\tau_0}\right] \tag{D.4}$$

for small fitting parameter b (the exponential empirical model was used since it produced a lower error). The exponential decay of the anomaly be^{-t/τ_0} is consistent generally with the exponential decay associated with solutions for simple viscoelastic models for initial value problems [90,91], under the assumption that the non-exponential part of the emission is proportional to the (creep) strain rate.

Appendix D.4. Phonon emission by moving dislocations

At high velocity dislocations radiate THz phonons efficiently [92], which perhaps might provide the beginning of a connection with up-conversion models discussed in the Introduction. However, the level of stress present in the May 20 experiment is insufficient to produce dislocation velocities sufficiently fast as to get to the stress regime where high rates of phonon emission occur. At lower dislocation velocity part of the friction is due to interaction with phonons, so that while THz phonon emission is inefficient, there is substantial coupling to and scattering with high-frequency phonon modes [93–95].

Appendix D.5. Creep in steel, and in other materials

Once our focus turned to creep in the experiment, we immediately presumed that creep in the steel in the vicinity of the Co-57 was most important. However, we might expect creep to be present in the wood clamps, epoxy, or ultrasonic coupling gel, where creep can be induced much more readily. THz phonons generated in the epoxy in general are more distant (and less likely to be important), except for the surface layer in contact with the Co-57 residue and steel. Creep in the wood or gel is sufficiently distant that one might expect it to impact the region of the Co-57 only indirectly.

Friction effects generally between the steel, residue and epoxy are likely important in generating very high frequency vibrations that could produce the effects observed.

Appendix E. Possibilities for Future Experimentation

The non-exponential decay observed at early time in the Fe-57 14.4 keV line, and in the Fe K_α and K_β X-rays, if real and if connected with phonon–nuclear coupling, potentially opens the door to a wide range of new experiments. In this appendix we consider some possibilities.

Appendix E.1. Studying excitation transfer

If we are able to delocalize nuclear excitation perhaps at the millimeter scale through excitation transfer with only modest levels of THz phonons from creep, then perhaps delocalization over larger distances is possible with more THz phonons. This could be studied with an energy dispersive X-ray camera.

Over what range can excitation transfer work? For example, suppose we put in a barrier layer of iron that is depleted in Fe-57, could we reduce excitation transfer through it, or stop it completely? The same approach could be used with a barrier layer made of a different material.

Would we get a much stronger version of the effect if we worked with a sample made of Fe-57?

Can the effect be seen using other low energy transitions? One candidate is the 6.237 keV E1 transition in Ta-181, which is longer lived, which should be helpful for the development of coherent effects. Another is the 1.565 keV M1+E2 transition in Hg-201, which has the advantage of a lower energy nuclear transition.

We would expect larger Dicke factors to be associated with excitation transfer in the event that most of the participating nuclei are initialized in the same ground state. This suggests that we might want to work with a strong magnetic field and low temperature, or perhaps a magnetized sample at low temperature.

Excitation transfer can be resonant, or non-resonant, which would make a difference in terms of angular anisotropy or beam formation in a material with aligned crystal planes. Is it possible to control the THz phonons in such a way as to maximize resonant excitation transfer and hence maximize the anisotropy?

Appendix E.2. Possibility of observing subdivision

Excitation transfer requires the least amount of phonon exchange of the relevant mechanisms reviewed in Section 2, which is why we have focused on excitation transfer mechanisms in connection with the May 20 experiment. Subdivision in the models requires coherent energy exchange, which makes it more challenging than excitation transfer, but the amount of energy exchange is less than for up-conversion. The demonstration of a subdivision effect would be extremely important, in that it would show that coherent energy exchange is possible.

Finding good resonances can minimize the energy mismatch and is a key issue for subdivision. A list of candidates relevant to experiments involving a Co-57 source is given in Table 3.

Table 3. Candidates for subdivision driven by a Co-57 source

Initial isotope	Energy (keV)	Final isotope	Energy (keV)	ΔN	Mismatch (keV)
Fe-57	136.4743	Sc-45	12.40	11	0.07
Fe-57	136.4743	Ta-181	136.262	1	0.212
Fe-57	14.4129	Hg-201	1.565	9	0.328
Fe-57	136.4743	Hg-201	1.565	87	0.340
Fe-57	136.4743	Os-186	137.159	1	–0.685
Fe-57	136.4743	Ta-181	6.237	22	–0.74

The lowest mismatch among the candidates is for

$$^{57}\text{Fe}(136.47) + 11\ ^{45}\text{Sc}(0) \quad \leftrightarrow \quad ^{57}\text{Fe}(0) + 11\ ^{45}\text{Sc}(12.40) + 0.07\ \text{keV}.$$

An experiment to demonstrate subdivision might involve the evaporation of radioactive Co-57 solution onto a steel plate, while at the same time evaporating scandium chloride in solution.

Non-resonant excitation transfer from the 136.47 keV state of Fe-57 might be possible to the 136.262 keV of Ta-181 according to

$$^{57}\text{Fe}(136.47) + ^{181}\text{Ta}(0) \quad \leftrightarrow \quad ^{57}\text{Fe}(0) + ^{181}\text{Hg}(136.262) + 0.212\ \text{keV}.$$

The energy mismatch is 212 eV, which is one of the lower mismatches among the candidates in Table 3. There is also a subdivision possible from the 136.47 keV state of Fe-57 to the 6.237 keV state of Ta-181

$$^{57}\text{Fe}(136.47) + 22\ ^{181}\text{Ta}(0) \quad \leftrightarrow \quad ^{57}\text{Fe}(0) + 22\ ^{181}\text{Hg}(6.237) - 0.74\ \text{keV}.$$

These two could be distinguished since non-resonant excitation transfer would result in Ta K_α X-ray emission; but no Ta K_α emission would be associated with subdivision – instead we would expect to see M-shell emission lines.

Another interesting possibility is to attempt the subdivision of the Fe 14.4 keV state to produce excitation of the 1565 eV state in ^{201}Hg according to

$$^{57}\text{Fe}(14.41) + 9\ ^{201}\text{Hg}(0) \quad \leftrightarrow \quad ^{57}\text{Fe}(0) + 9\ ^{201}\text{Hg}(1.565) + 0.33\ \text{keV}.$$

The energy mismatch is about 330 eV, which is again one of the lower mismatches in the table.

We had entertained the possibility that subdivision might account for the enhanced emission at early time in the May 20 experiment. Subdivision of the 136.5 keV state to the 14.4 keV state would be described by

$$^{57}\text{Fe}(136.47) + 9\ ^{57}\text{Fe}(0) \quad \leftrightarrow \quad ^{57}\text{Fe}(0) + 9\ ^{57}\text{Fe}(14.421) + 6.76\ \text{keV}.$$

The relatively large energy mismatch, combined with the short (8.7 ns) half-life of the 136.5 keV state, suggests that this process would not be favored in the May 20 experiment. If this process were dominant, we would have seen a reduction in the Sn-K_α proxy for the harder 122 keV and 136 keV along with increased 14.4 keV and Fe K_α emission. Due to the relative absence of a decrease in the Sn K_α signal at early time in the data we consider this subdivision mechanism as unlikely to account for the observations reported in this paper.

Appendix E.3. Issues associated with up-conversion experiments

Our interest in up-conversion and down-conversion come from our interpretation of several anomalies in Condensed Matter Nuclear Science. The excess heat effect in the Fleischmann–Pons experiment would not be anomalous if there were a down-conversion mechanism established consistent with the models we have developed. Collimated X-ray emission in the Karabut experiment would not be anomalous if there were an up-conversion mechanism accepted. As mentioned above, up-conversion and down-conversion are described by the same basic models, so a demonstration of up-conversion implies down-conversion can occur, and vice versa. We are interested in whether the predicted up-conversion and down-conversion mechanisms can be demonstrated experimentally. Note that the experimental demonstration of a subdivision effect would strongly support the notion that up-conversion and down-conversion can work.

One candidate hypothesis for the early time enhancement in the May 20 experiment is up-conversion, which we have considered seriously in connection with the May 20 experiment. According to theory up-conversion would occur as a result of a great many non-resonant excitation transfer events before the transition decoheres. If so, then we would like to see unambiguous evidence for excitation transfer first, which is why our interest focuses on candidate

hypotheses involving excitation transfer first. Arguing against an up-conversion mechanism is that similar experiments carried out with no Co-57 do not show reproducible emission in the scintillator/PMT detector.

For future up-conversion experiments we consider working with a low-energy transition (such as the 1.565 keV transition in Hg-201 or the 6.237 keV transition in Ta-181) [4], and then follow the model which points to the importance of: the number of identical nuclei involved in the ground state; maximization of the number of optical phonons in a mode that is spatially uniform; maximization of the half-life of the upper and lower states; ensuring that loss is present (which is thought to be dealt with in the low-Q resonator modes of optical phonons). These same issues should be relevant for similar reasons for subdivision and for excitation transfer.

Acknowledgments

We appreciate help from Associate Director Mitch Galanek of the MIT Office of Environment, Health and Safety who provided much technical assistance, especially in connection with the acquisition of the ^{57}Co, the evaporation of the radioactive solution on the plate, and with covering it with epoxy. He also arranged for calibrations sources used for our detectors, and lab space for the experiment. Professor Cardinal Warde has kindly let us use some of his lab space for this research, which we very much appreciate. Dewey Weaver provided much appreciated encouragement. Industrial Heat provided support for F. Metzler and S. Lu, and for some of the detectors, which made the experiments possible. We very much appreciate encouragement from Prof. I. Chaudhary of the University of Engineering and Technology in Lahore, along with many hours of helpful technical discussions. We acknowledge review comments of an earlier draft from Graham Hubler. Helpful discussions with Malcolm Fowler are much appreciated.

References

[1] M. Fleischmann and S. Pons, Electrochemically induced nuclear fusion of deuterium, *J. Electroanal. Chem. and Interfacial Electrochem.* **261** (1989) 301–308.

[2] M. Fleischmann, S. Pons, M. W. Anderson, L. J. Li, and M. Hawkins, Calorimetry of the palladium–deuterium–heavy water system, *J. Electroanal. Chem. and Interfacial Electrochem.* **287** (1990) 293–348.

[3] E. Storms, *Science of Low Energy Nuclear Reaction: A Comprehensive Compilation of Evidence and Explanations about Cold Fusion*, World Scientific, New Jersey, USA, 2004.

[4] P.L. Hagelstein, Bird's Eye View of Phonon Models for Excess Heat in the Fleischmann–Pons Experiment, *J. Condensed Matter Nucl. Sci.* **6** (2011) 169.

[5] P.L. Hagelstein, Quantum composites: A review, and new results for models for Condensed Matter Nuclear Science, *J. Condensed Matter Nuclear Science* **20** (2016) 139–225.

[6] P.L. Hagelstein and I.U. Chaudhary. Phonon models for anomalies in condensed matter nuclear science, *Current Science* **108** (2015) 507.

[7] P.L. Hagelstein, Current status of the theory and modeling effort based on fractionation, *J. Condensed Matter Nucl. Sci.* **19** (2016) 98–109.

[8] P.L. Hagelstein, Directional X-ray and gamma emission in experiments in condensed matter nuclear science, *Current Science* **108** (2015) 601.

[9] A.B. Karabut, Research into powerful solid X-ray laser (wave length is 0.8–1.2nm) with excitation of high current glow discharge ions, *Proc. 11th Int. Conf. on Emerging Nuclear Energy Systems*, 29 September–4 October 2002, Albuquerque, New Mexico, USA, pp. 374–381.

[10] A.B. Karabut, Experimental research into characteristics of X-ray emission from solid-state cathode medium of high-current glow discharge, *Proc. 10th Int. Conf. on Cold Fusion*, August 24–29, 2003, Cambridge, MA, USA.

[11] A.B. Karabut, Research into characteristics of X-ray emission laser beams from solid-state cathode medium of high current glow discharge, *Proc. 11th Int. Conf. on Cold Fusion*, 31 October–5 November, 2004, France, pp. 253–257.

[12] A.B. Karabut, Study of energetic and temporal characteristics of X-ray emission from solid state cathode medium of high current glow discharge, *Proc. 12th Int. Conf. on Cold Fusion*, December 2–7, 2006, Japan, pp. 344–350.

[13] A.B. Karabut, E.A. Karabut, Research into energy spectra of X-ray emission from solid cathode medium during the high current glow discharge operation and after the glow discharge current switch off, *Proc. 14th Int. Conf. on Cold Fusion*, August 10–15, 2008, USA.
[14] A.B. Karabut and E.A. Karabut, Study of deuterium loading into Pd cathode samples of glow discharge, *Proc. of 9th Int. Workshop on Anomalies in Hydrogen/Deuterium Gas Loaded Metals*, 6–11 September 2010, Siena, Italy.
[15] A.B. Karabut, E.A. Karabut and P.L. Hagelstein, Spectral and temporal characteristics of X-ray emission from metal electrodes in a high-current glow discharge, *J. Condensed Matter Nucl. Sci.* **6** (2012) 217.
[16] A.B. Karabut and E.A. Karabut, Research into excited 0.6–6.0 keV energy levels in the cathode solid medium of glow discharge by X-ray spectra emission, *J. Condensed Matter Nucl. Sci.* **8** (2012) 159.
[17] A.B. Karabut, Research into excited long lived 0.6–6.0 keV energy levels in the cathode solid medium of glow discharge by x-Ray spectra emission, *J. Materials Sci. Eng. B* **3** (2013) 298.
[18] A.A. Kornilova, V.I. Vysotskii, N.N. Sysoev, N.K. Litvin, V.I. Tomak and A.A. Barzov, Generation of intense X-rays during ejection of a fast water jet from a metal channel to atmosphere, *J. Surface Investigation: X-ray, Synchrotron and Neutron Techniques* **4** (2010) 1008–1017.
[19] A.A. Kornilova, V.I. Vysotskii, N.N. Sysoev, N.K. Litvin, V.I. Tomak and A.A. Barzov, Shock-cavitational mechanism of X-ray generation during fast water stream cavitation, *Moscow University Phys. Bulletin* **65** (2010) 46–50.
[20] V.I. Vysotskii, A.A. Kornilova and A. O. Vasilenko, Observation and investigation of X-ray and thermal effects at cavitation, *Current Science* **108** (2015) 114.
[21] V.I. Vysotskii, A.A. Kornilova, A. O. Vasilenko and V.I. Tomak, Detection and investigation of undamped temperature waves excited under water jet cavitation, *J. Surface Investigation. X-ray, Synchrotron and Neutron Techniques* **8** (2014) 1186–1192.
[22] V.I. Vysotskii, A.A. Kornilova, A. O. Vasilenko, T. B. Krit and M. V. Vysotskyy, The prediction, observation and study of long-distant undamped thermal waves generated in pulse radiative processes, *Nucl. Instr. Meth. Phys. Res. Section B: Beam Interactions with Materials and Atoms* (2017).
[23] P.L. Hagelstein and I.U. Chaudhary, Coupling between the center of mass and relative degrees of freedom in a relativistic quantum composite and applications, *J. Condensed Matter Nucl. Sci.* **24** (2017) 117–122.
[24] F. Cardone, R. Mignani, M. Monti, A. Petrucci and V. Sala, Piezonuclear neutrons from iron, *Modern Phys. Lett. A* **27** (2012) 1250102.
[25] F. Cardone and S. Duro, Anisotropy angle of the DST-emissions, *Modern Phys. Lett. B* **28** (2014) 1450156.
[26] G. Albertini, V. Calbucci and F. Cardone, Statistics of piezonuclear emissions: early results, *Modern Phys. Lett. B* **28** (2014) 1450036.
[27] F. Cardone, G. Cherubini, M. Lammardo, R. Mignani, A. Petrucci, A. Rosada, V. Sala and E. Santoro, Violation of local Lorentz invariance for deformed space–time neutron emission, *Eur. Phys. J. Plus* **130** (2015) 55–65.
[28] F. Cardone and A. Rosada, Energy spectra and fluence of the neutrons produced in deformed space–time conditions, *Modern Phys. Lett. B* **30** (2016) 1650346.
[29] F. Cardone, A. Manuello, R. Mignani, A. Petrucci, E. Santoro, M. Sepielli and A. Carpinteri, Ultrasonic piezonuclear reactions in steel and sintered ferrite bars, *J. Adv. Phys.* **5** (2016) 69–75.
[30] G. Albertini, V. Calbucci, F. Cardone, G. Fattorini, R. Mignani, A. Petrucci, F. Ridolfi and A. Rotili, Evidence of alpha emission from compressed steel bars, *Int. J. Modern Phys. B* **27** (2013) 1350124.
[31] F. Cardone, V. Calbucci and G. Albertini, Possible evidence of piezonuclear alpha emission, *J. Advanced Phys.* **2** (2013) 20–24.
[32] F. Cardone, V. Calbucci and G. Albertini, Deformed space–time of the piezonuclear emissions, *Modern Phys. Lett. B* **28** (2014) 1450012.
[33] F. Cardone, A. Petrucci and A. Rosada, Isotopical changes induced by ultrasounds in iron, *Int. J. Modern Phys. B* **28** (2014) 1450107.
[34] G. Albertini, F. Cardone, M. Lammardo, A. Petrucci, F. Ridolfi, A. Rosada, V. Sala and E. Santoro, Atomic and isotopic changes induced by ultrasounds in iron, *J. Radioanal. Nucl. Chem.* **304** (2015) 955–963.
[35] F. Cardone, M. Lammardo, A. Petrucci, A. Rosada and E. Santoro, Isotopical changes in piezonuclear iron, *J. Adv. Phys.* **5** (2016) 90–96.
[36] G. Albertini, V. Calbucci, F. Cardone and A. Petrucci, Piezonuclear reactions and DST-reactions, *Materials and Processes*

for Energy: Communicating Current Research and Technological Developments, A. Mendez-Vilas (Ed.), 2013, pp. 769–780.
[37] G. Albertini, L. Kostro and F. Cardone, Deformed Space–Time Reactions, *Unified Field Mechanics: Natural Science Beyond the Veil of Spacetime-Proc. IX Symposium Honoring Noted French Mathematical Physicist Jean-Pierre Vigier* R.L. Amoroso et al. (Eds.), World Scientific, NJ, USA, 2016, pp. 157–163.
[38] F.L. Tanzella, P.L. Hagelstein, J. Bao and M.C.H. McKubre, Progress report on an experiment to clarify collimated X-ray emission in Karabutï£¡s experiment, *X-Ray Lasers 2014*, Springer, Berlin, 2016, pp. 115–120.
[39] F.L. Tanzella, J. Bao, M.C.H. McKubre and P.L. Hagelstein, Seeking X-rays and charge emission from a copper foil driven at MHz frequencies, *J. Condensed Matter Nucl. Sci.* **19** (2016) 110–118.
[40] F. Metzler, P.L. Hagelstein and S. Lu, Developing phononï£¡nuclear coupling experiments with vibrating plates and radiation detectors, *J. Condensed Matter Nucl. Sci.* **24** (2017) 98–113.
[41] D.E. Alburger and M.A. Grace, The Disintegration of Cobalt 57, *Proc. Phy. Soc. Section A* **67** (1954) 280–283.
[42] B. Crasemann and D.L. Manley, Radioactivity of Co^{57}, *Phy. Rev.* **98** (1955) 66–68.
[43] J.M. Cork, M.K. Brice and L.C. Schmid, Energies of the radiations from Co^{57} and Co^{58}, *Phy. Rev.* **99** (1955) 703–705.
[44] A.T.G. Ferguson, M.A. Grace and J.O. Newton, The decay of the 136 keV level in Fe^{57}, *Nucl. Phys.* **17** (1960) 9–15.
[45] V.P. Chechev and N.K. Kuzmenko, CEA Table de radiounucléides ^{57}Co, Laboratoire National Henri Becquerel LNE-LNHB/CEA Report (2014).
[46] O.C. Kistner and A.W. Sunyar, Excited states of ^{57}Fe populated in ^{57}Co decay, *Phy. Rev.* **139** (1965) B 295–B 299.
[47] G.D. Sprouse and S.S. Hanna, Gamma ray transitions in ^{57}Fe, *Nucl. Phys.* **74** (1965) 177–183.
[48] S.B. Garfinkel and J.M.R. Hutchinson, The standardization of cobalt-57, *Int. J. Appl. Radiation and Isotopes* **17** (1966) 587–593.
[49] M.E.C. Troughton, The absolute standardization of cobalt-57, *Int. J. Appl. Radiation and Isotopes* **17** (1966) 145–150.
[50] W. Rubinson and K.P. Gopinathan, Conversion coefficients of the Fe^{57} 14.4-keV transition, the K-capture fraction in Co^{57} e^- capture and the K-fluorescence yield of Fe, *Phy. Rev.* **170** (1968) 969.
[51] A.V. Simakin and G.A. Shafeev, Initiation of Nucl. reactions under laser irradiation of Au nanoparticles in the aqueous solution of uranium salt, *Appl. Phys. A* **101** (2010) 199–203.
[52] A.V. Simakin and G.A. Shafeev, Effect of laser irradiation of nanoparticles in aqueous uranium salt solutions on nuclide activity, *Quantum Electron.* **41** (2011) 614.
[53] A.V. Simakin and G.A. Shafeev, Accelerated alpha-decay of uranium isotopes induced by exposure of aqueous solution of uranium salt with gold nanoparticles to laser radiation, *Phys. Wave Phenomena* **21** (2013) 31–37.
[54] E.V. Barmina, I.A. Sukhov, N.M. Lepekhin, Yu S. Priseko, V.G. Filippov, A.V. Simakin and G.A. Shafeev, Application of copper vapour lasers for controlling activity of uranium isotopes, *Quantum Electron.* **43** (2013) 591–596.
[55] E.V. Barmina, A.V. Simakin and G.A. Shafeev, Laser-induced caesium-137 decay, *Quantum Electron.* **44** (2014) 791–792.
[56] S.N. Andreev, The nonlinear quenching of the radioactivity of cesium-137, *All-Russian Scientific Forum of Young Scientists "Science of the future – the young science"*, Kazan, Sept. 20–23, 2016.
[57] A. Carpinteri, F. Cardone and G. Lacidogna, PiezoNucl. neutrons from brittle fracture: early results of mechanical compression tests, *Strain* **45** (2009) 332–339.
[58] A. Carpinteri, F. Cardone and G. Lacidogna, Energy emissions from failure phenomena: mechanical, electromagnetic, nuclear, *Experimental Mechanics* **50** (2010) 1235–1243.
[59] A. Carpinteri, G. Lacidogna, A. Manuello and Oscar Borla, PiezoNucl. fission reactions from earthquakes and brittle rocks failure: evidence of neutron emission and non-radioactive product elements, *Experimental Mechanics* **53** (2013) 345–365.
[60] P.L. Hagelstein, Probabilistic models for beam, spot and line emission for collimated X-ray emission in the Karabut experiment, *J. Condensed Matter Nucl. Sci.* **22** (2017) 53–73.
[61] P.L. Hagelstein and I.U. Chaudhary, Energy exchange in the lossy spin–boson model, *J. Condensed Matter Nucl. Sci.* **5** (2011) 52.
[62] P.L. Hagelstein and I.U. Chaudhary, Second-order formulation and scaling in the lossy spin–boson model, *J. Condensed Matter Nucl. Sci.* **5** (2011) 87.
[63] P.L. Hagelstein and I.U. Chaudhary, Local approximation for the lossy spinï£¡-boson model, *J. Condensed Matter Nucl. Sci.* **5** (2011) 102.
[64] P.L. Hagelstein and I.U. Chaudhary, Coherent energy exchange in the strong coupling limit of the lossy spin–boson model,

J. Condensed Matter Nucl. Sci. **5** (2011) 116.
[65] V.J. Minkiewicz, G. Shirane and R. Nathans, Phonon dispersion relation for iron, *Phy. Rev.* **162** (1967) 528.
[66] H.Y. Erbil, Evaporation of pure liquid sessile and spherical suspended drops: A review, *Adv. Colloid and Interface Sci.* **170** (2012) 67–86.
[67] R.D. Deegan, O. Bakajin, T.F. Dupont, G. Huber, S.R. Nagel and T.A. Witten, Contact line deposits in an evaporating drop, *Phys. Rev. E* **62** (2000) 756–765.
[68] N. Shahidzadeh, M.F.L. Schut, J. Desarnaud, M. Prat and D. Bonn, Salt stains from evaporating droplets, *Scientific Reports* **5** (2015) 10335.
[69] V.E. Nakoryakov, S.Ya. Misyura and S.L. Elistratov, Non-isothermal desorption of droplets of complex composition, *Thermal Sci.* **16** (2012) 997–1004.
[70] D. Pacella, A. Romano, S.H. Lee, F. Causa, L. Gabellieri and W. Choe, Self-consistent calibration of detectors and sources for hard and soft X-ray diagnostics, *Modern Instrumentation* **3** (2014) 13–23.
[71] R.L. Roderick and R. Truell, The measurement of ultrasonic attenuation in solids by the pulse technique and some results in steel, *J. Appl. Phys.* **23** (1952) 267–279.
[72] K. Kamigaki, Ultrasonic attenuation in steel and cast iron, *Science reports of the Research Institutes, Tohoku University. Ser. A, Phys. , Chemistry and Metallurgy* **9** (1957) 48–77.
[73] J.-D. Aussel and J.-P. Monchalin, Measurement of ultrasound attenuation by laser ultrasonics, *J. Appl. Phys.* **65** (1989) 2918–2922.
[74] R.M. Goldhoff, Uniaxial creep-rupture behavior of low-alloy steel under variable loading conditions, *Trans. AMSE, J. Basic Eng.* **87** (1965) 374–378.
[75] L.J. Cuddy, Internal stresses and structures developed during creep, *Metallurgical and Materials Trans. B* **1** (1970) 395–401.
[76] E. Krempl, An experimental study of room-temperature rate-sensitivity, creep and relaxation of AISI type 304 stainless steel, *J. Mechanics Phys. Solids* **27** (1979) 363–375.
[77] L.A. Deibler, Room temperature creep in metals and alloys, *Sandia National Lab Report* No. SAND2014-17935 (2014).
[78] P. Gressel, Untersuchungen ï£¡ber das Zeitstandbiegeverhalten von Holzwerkstoffen in Abhï£¡ngigkeit von Klima und Belastung, it Eur. J. Wood and Wood Products **30** (1972) 347–355.
[79] S.J. Smulski, Creep functions for wood composite materials, *Wood and Fiber Sci.* **21** (1989) 45.
[80] D.E. Lyon and A.P. Schniewind, Prediction of creep in plywood Part I. Prediction models for creep in plywood, *Wood Fiber Sci.* **10** (2007) 28–38.
[81] M. Peach and J.S. Koehler, The forces exerted on dislocations and the stress fields produced by them, *Phy. Rev.* **80** (1950) 436.
[82] D. Caillard, Kinetics of dislocations in pure Fe. Part I. In situ straining experiments at room temperature, *Acta Materialia* **58** (2010) 3493–3503.
[83] A.P.L. Turner and T. Vreeland, The effect of stress and temperature on the velocity of dislocations in pure iron monocrystals, *Acta metallurgica* **18** (1970) 1225–1235.
[84] M.S. Duesbery, The influence of core structure on dislocation mobility, *Phil. Magazine* **19** (1969) 501–526.
[85] F. Louchet, L.P. Kubin and D. Vesely, In situ deformation of bcc crystals at low temperatures in a high-voltage electron microscope dislocation mechanisms and strain-rate equation, *Phil. Magazine A* **39** (1979) 433–454.
[86] E. Orowan, Problems of plastic gliding, *Proc. Phy. Soc.* **52** (1940) 8.
[87] A.S. Krausz, The activation volume associated with the plastic deformation of ice, *Appl. Sci. Res.* **26** (1972) 86–92.
[88] E. Nadgornyi, Dislocation dynamics and mechanical properties of crystals, *Progr. Materials Sci.* **31** (1988) 1–530.
[89] T.Y. Gorazdovskii, Hard radiation from solids failing in shear, *JETP Lett.* **5** (1967) 64–67.
[90] D. Roylance, Engineering viscoelasticity, Course notes, Dept. of Materials Science and Engineering, Massachusetts Institute of Technology, 200, pp. 11–37.
[91] F. Mainardi and G. Spada, Creep, relaxation and viscosity properties for basic fractional models in rheology, *Eur. Phy. J. – Special Topics* **193** (2011) 133–160.
[92] J. Marian and A. Caro, Moving dislocations in disordered alloys: Connecting continuum and discrete models with atomistic simulations, *Phy. Rev. B* **74** (2006) 024113. See Fig. 12.

[93] J. Lothe, Theory of dislocation motion in pure slip, *J. Appl. Phys.* **33** (1962) 2116–2125.
[94] J.D. Eshelby, The interaction of kinks and elastic waves, *Proc. Roy. Soc. (London). Series A, Mathematical and Physical Sciences* **A266** (1962) 222–246.
[95] A. Hikata, R.A. Johnson and C. Elbaum. Interaction of dislocations with electrons and with phonons, *Phy. Rev. B* **2** (1970) 4856–4863.